A.

B.

Fig. 5. Effects of Hsp40 and/or Hsp70 on in vitro tau self-assembly (solid squares). **A:** Heparin-induced tau aggregation was assessed by measuring ThT fluorescence at the indicated time points (mean ± SD; n = 5). Hsp40 (diamonds), Hsp70 (triangles), and Hsp40 + Hsp70 (open squares) were added to the aggregation reaction mixture at time zero. **B:** Tau aggregation levels are shown as a function of ThT fluorescence intensity (mean ± SD; n = 5). Tau was incubated with heparin in the presence of Hsp40, Hsp70, or Hsp40 + Hsp70 at the indicated concentrations for 147 hr.

ble tau to insoluble tau having a β-sheet conformation remain unclear. Recent studies have suggested the involvement of multiple degradation pathways in this process that require the action of molecular chaperones (Dou et al., 2003; Petrucelli et al., 2004). Here, we found that molecular chaperone-mediated tau protein metabolism plays a possible role in converting soluble tau to granular tau oligomer (intermediates of tau filaments) in human brain. Indeed, the levels of TBS-soluble tau correlated well with those of Hsp90, Hsp40, Hsp27, α-crystallin, and CHIP. In contrast to the levels of TBS-soluble tau, the levels of granular tau oligomer were inversely proportional to those of HSPs. In addition, our in vitro study showed that Hsp40 and Hsp70 proteins prevented tau aggregation. Taken together, these findings indicate that a molecular chaperone-tau

protein processing pathway likely controls the initial phase of tau aggregation.

Together with comparative biochemical analyses of tau aggregates, electrophoretic profiles of pathological tau protein have allowed the molecular classification of tauopathies. Indeed, tauopathies differ in both tau phosphorylation and tau isoform content (Lee et al., 2001; Sergeant et al., 2005). Although electrophoretic tau protein profiles in various tauopathies have been well characterized, variations in tau protein levels have not been examined extensively, because studies of autopsy samples can be complicated by variability in disease severity, agonal state, age, environmental factors, and post-mortem delays. In the present study, we observed that TBS-soluble tau levels varied across different Braak stages, whereas β-actin, GAPDH, and NSE levels remained steady across different Braak stages. Moreover, the levels of TBS-soluble tau correlated well with those of Hsp90, Hsp40, Hsp27, α-crystallin, and CHIP. These variations were not related to post-mortem interval times, so it was unlikely that these protein levels were affected by post-mortem interval. In addition to chaperone protein levels, Akt and β-tubulin levels also positively correlated with TBS-soluble tau levels. Akt is known to be an Hsp90 client protein (Basso et al., 2002), and β-tubulin is known to be a component of microtubules that are stabilized by tau protein. Therefore, Akt, β-tubulin, and tau protein levels may also be regulated by the chaperone complex through a similar processing pathway.

Recently, our group described the quantitative analysis of a granular-shaped prefilamentous form of tau, the granular tau oligomer, in human brain (Maeda et al., 2006, 2007). We observed increased levels of granular tau oligomer in the frontal cortices staged at Braak I, suggesting that tau dysfunction had already occurred in frontal cortex by the time NFTs formed in entorhinal cortex. In the present study, we observed an inverse correlation between granular tau oligomer and HSP levels, the latter of which positively correlated with soluble tau protein levels. This inverse correlation was more significant when Braak 0 samples were excluded from our analysis. Braak NFT staging traces the gradual development of neurofibrillary changes in brain (Braak and Braak, 1991; Braak et al., 1994). Stage I is characterized by neurodegeneration of specific projection cells in the transentorhinal region, whereas Braak 0 is characterized by the absence of NFTs. Although we did not detect NFTs in the frontal cortices of Braak 0 and Braak I brains, the levels of granular tau oligomer and Hsp27 in Braak I samples were elevated. Because Hsp27 preferentially interacts with a hyperphosphorylated tau variant in human samples (Shimura et al., 2004a), it is possible that hyperphosphorylated prefilamentous tau was already induced in the frontal cortices of Braak I brains. With regard to the inverse correlation between granular tau oligomer and HSP levels, reduction of stress response can explain the increase in granular tau oligomers after the start of neurofibrillary changes. Because aging is a risk factor for various neurodegenerative disorders,

including AD, and the aging process is associated with gradual accumulation of oxidative stress factors (Coyle and Puttfarcken, 1993), it seems reasonable that the overriding of oxidative insults disables molecular chaperones.

Dickey et al. (2006a) reported that HSP induction mediates proteasome-dependent tau degradation. They found that Hsp90 inhibitors reduced the levels of tau phosphorylated at proline-directed Ser/Thr sites (pS202/ T205, pS396/S404) and conformationally altered (MC-1) tau species that are induced by Hsp70, Hsp40, and Hsp27. Although Dickey et al. used an in vitro experimental system comprising P301L mutated tau-expressing H4 and CHO cells (Dickey et al., 2006a), a system that is completely different from our in vivo experimental system involving the protein profiling of human brains, Dickey et al.'s data were consistent with our results showing an inverse correlation between HSPs and MC-1-immunoreactive granular tau oligomers (Maeda et al., 2007). Still, we do not know whether the activation of multiple chaperone systems or inactivation of Hsp90 is induced by stress responses that occur during brain aging. However, because Hsp90 client proteins, such as Akt, are also related to HSP levels in human brain, it is likely that the Hsp90 chaperoning cycle mediates tau protein metabolism. Results from coimmunoprecipitation and in vitro tau assembly assays demonstrated that physiological interactions occur between tau and Hsp70. Hsp70 is well known to be a prominent HSP in eukaryotic cytosol (Hartl and Hayer-Hartl, 2002). Hsp70 function not only is modulated by Hsp40 to initiate protein refolding but is also associated with CHIP to process the ubiquitin-proteasome pathway (Dickey et al., 2007). Therefore, it seems likely that Hsp70 is also involved in chaperone-mediated tau protein metabolism.

Tau protein has been reported to be a substrate for a number of proteases, such as trypsin, chymotrypsin, cathepsin D, calpains, caspases, proteasomal proteases, and thrombin. Decreased proteasome activity in AD brains has been previously reported (Keller et al., 2000; Lopez Salon et al., 2000; Keck et al., 2003). The inhibition of Hsp90-mediated tau clearance by a proteasomal inhibitor has been also reported (Dickey et al., 2006a). The lysosomal pathway may represent a secondary pathway for HSP-mediated tau degradation. An alternative tau degradation pathway is chaperone-mediated autophagy (CMA). Recently, α-synuclein has been shown to be a substrate for CMA (Cuervo, 2004) and to be modulated by cochaperone CHIP for degradation via CMA (Shin et al., 2005). Our findings strongly suggest that molecular chaperone-mediated tau protein metabolism is a major regulator of the formation of abnormal oligomeric complexes of tau. Therefore, molecular chaperones might be promising targets in the development of therapeutics for diseases characterized by neurofibrillary degeneration as well as for other diseases characterized by protein conformational disorders. Further studies are necessary to determine the precise status of tau protein as a molecular chaperone client.

REFERENCES

Alonso AC, Grundke-Iqbal I, Iqbal K. 1996. Alzheimer's disease hyperphosphorylated tau sequesters normal tau into tangles of filaments and disassembles microtubules. Nat Med 2:783–787.

Arriagada PV, Growdon JH, Hedley-Whyte ET, Hyman BT. 1992. Neurofibrillary tangles but not senile plaques parallel duration and severity of Alzheimer's disease. Neurology 42:631–639.

Basso AD, Solit DB, Chiosis G, Giri B, Tsichlis P, Rosen N. 2002. Akt forms an intracellular complex with heat shock protein 90 (Hsp90) and Cdc37 and is destabilized by inhibitors of Hsp90 function. J Biol Chem 277:39858–39866.

Braak E, Braak H, Mandelkow EM. 1994. A sequence of cytoskeleton changes related to the formation of neurofibrillary tangles and neuropil threads. Acta Neuropathol 87:554–567.

Braak H, Braak E. 1991. Neuropathological staging of Alzheimer-related changes. Acta Neuropathol 82:239–259.

Coyle JT, Puttfarcken P. 1993. Oxidative stress, glutamate, and neurodegenerative disorders. Science 262:689–695.

Cuervo AM. 2004. Autophagy: in sickness and in health. Trends Cell Biol 14:70–77.

Dabir DV, Trojanowski JQ, Richter-Landsberg C, Lee VM, Forman MS. 2004. Expression of the small heat-shock protein alphaB-crystallin in tauopathies with glial pathology. Am J Pathol 164:155–166.

Dickey CA, Dunmore J, Lu B, Wang JW, Lee WC, Kamal A, Burrows F, Eckman C, Hutton M, Petrucelli L. 2006a. HSP induction mediates selective clearance of tau phosphorylated at proline-directed Ser/Thr sites but not KXGS (MARK) sites. FASEB J 20:753–755.

Dickey CA, Yue M, Lin WL, Dickson DW, Dunmore JH, Lee WC, Zehr C, West G, Cao S, Clark AM, Caldwell GA, Caldwell KA, Eckman C, Patterson C, Hutton M, Petrucelli L. 2006b. Deletion of the ubiquitin ligase CHIP leads to the accumulation, but not the aggregation, of both endogenous phospho- and caspase-3-cleaved tau species. J Neurosci 26:6985–6996.

Dickey CA, Kamal A, Lundgren K, Klosak N, Bailey RM, Dunmore J, Ash P, Shoraka S, Zlatkovic J, Eckman CB, Patterson C, Dickson DW, Nahman NS Jr, Hutton M, Burrows F, Petrucelli L. 2007. The high-affinity HSP90-CHIP complex recognizes and selectively degrades phosphorylated tau client proteins. J Clin Invest 117:648–658.

Dou F, Netzer WJ, Tanemura K, Li F, Hartl FU, Takashima A, Gouras GK, Greengard P, Xu H. 2003. Chaperones increase association of tau protein with microtubules. Proc Natl Acad Sci U S A 100:721–726.

Gamblin TC, Chen F, Zambrano A, Abraha A, Lagalwar S, Guillozet AL, Lu M, Fu Y, Garcia-Sierra F, LaPointe N, Miller R, Berry RW, Binder LI, Cryns VL. 2003. Caspase cleavage of tau: linking amyloid and neurofibrillary tangles in Alzheimer's disease. Proc Natl Acad Sci U S A 100:10032–10037.

Garcia-Sierra F, Ghoshal N, Quinn B, Berry RW, Binder LI. 2003. Conformational changes and truncation of tau protein during tangle evolution in Alzheimer's disease. J Alzheimers Dis 5:65–77.

Hartl FU, Hayer-Hartl M. 2002. Molecular chaperones in the cytosol: from nascent chain to folded protein. Science 295:1852–1858.

Hasegawa M, Smith MJ, Goedert M. 1998. Tau proteins with FTDP-17 mutations have a reduced ability to promote microtubule assembly. FEBS Lett 437:207–210.

Hatakeyama S, Matsumoto M, Kamura T, Murayama M, Chui DH, Planel E, Takahashi R, Nakayama KI, Takashima A. 2004. U-box protein carboxyl terminus of Hsc70-interacting protein (CHIP) mediates polyubiquitylation preferentially on four-repeat Tau and is involved in neurodegeneration of tauopathy. J Neurochem 91:299–307.

Imai Y, Soda M, Hatakeyama S, Akagi T, Hashikawa T, Nakayama KI, Takahashi R. 2002. CHIP is associated with Parkin, a gene responsible for familial Parkinson's disease, and enhances its ubiquitin ligase activity. Mol Cell 10:55–67.

Jicha GA, Berenfeld B, Davies P. 1999. Sequence requirements for formation of conformational variants of tau similar to those found in Alzheimer's disease. J Neurosci Res 55:713–723.

Katsuno T, Morishima-Kawashima M, Saito Y, Yamanouchi H, Ishiura S, Murayama S, Ihara Y. 2005. Independent accumulations of tau and amyloid beta-protein in the human entorhinal cortex. Neurology 64:687–692.

Keck S, Nitsch R, Grune T, Ullrich O. 2003. Proteasome inhibition by paired helical filament-tau in brains of patients with Alzheimer's disease. J Neurochem 85:115–122.

Keller JN, Hanni KB, Markesbery WR. 2000. Impaired proteasome function in Alzheimer's disease. J Neurochem 75:436–439.

Kuret J, Chirita CN, Congdon EE, Kannanayakal T, Li G, Necula M, Yin H, Zhong Q. 2005. Pathways of tau fibrillization. Biochim Biophys Acta 1739:167–178.

Lee VM, Goedert M, Trojanowski JQ. 2001. Neurodegenerative tauopathies. Annu Rev Neurosci 24:1121–1159.

Lopez Salon M, Morelli L, Castano EM, Soto EF, Pasquini JM. 2000. Defective ubiquitination of cerebral proteins in Alzheimer's disease. J Neurosci Res 62:302–310.

Maeda S, Sahara N, Saito Y, Murayama S, Ikai A, Takashima A. 2006. Increased levels of granular tau oligomers: an early sign of brain aging and Alzheimer's disease. Neurosci Res 54:197–201.

Maeda S, Sahara N, Saito Y, Murayama M, Yoshiike Y, Kim H, Miyasaka T, Murayama S, Ikai A, Takashima A. 2007. Granular tau oligomers as intermediates of tau filaments. Biochemistry 46:3856–3861.

Muchowski PJ, Wacker JL. 2005. Modulation of neurodegeneration by molecular chaperones. Nat Rev 6:11–22.

Nemes Z, Devreese B, Steinert PM, Van Beeumen J, Fesus L. 2004. Cross-linking of ubiquitin, HSP27, parkin, and alpha-synuclein by gamma-glutamyl-epsilon-lysine bonds in Alzheimer's neurofibrillary tangles. FASEB J 18:1135–1137.

Petrucelli L, Dickson D, Kehoe K, Taylor J, Snyder H, Grover A, De Lucia M, McGowan E, Lewis J, Prihar G, Kim J, Dillmann WH, Browne SE, Hall A, Voellmy R, Tsuboi Y, Dawson TM, Wolozin B, Hardy J, Hutton M. 2004. CHIP and Hsp70 regulate tau ubiquitination, degradation and aggregation. Hum Mol Genet 13:703–714.

Sahara N, Murayama M, Mizoroki T, Urushitani M, Imai Y, Takahashi R, Murata S, Tanaka K, Takashima A. 2005. In vivo evidence of CHIP up-regulation attenuating tau aggregation. J Neurochem 94:1254–1263.

Saito Y, Nakahara K, Yamanouchi H, Murayama S. 2002. Severe involvement of ambient gyrus in dementia with grains. J Neuropathol Exp Neurol 61:789–796.

Sato S, Tatebayashi Y, Akagi T, Chui DH, Murayama M, Miyasaka T, Planel E, Tanemura K, Sun X, Hashikawa T, Yoshioka K, Ishiguro K, Takashima A. 2002. Aberrant tau phosphorylation by glycogen synthase kinase-3beta and JNK3 induces oligomeric tau fibrils in COS-7 cells. J Biol Chem 277:42060–42065.

Schweers O, Mandelkow EM, Biernat J, Mandelkow E. 1995. Oxidation of cysteine-322 in the repeat domain of microtubule-associated protein tau controls the in vitro assembly of paired helical filaments. Proc Natl Acad Sci U S A 92:8463–8467.

Sergeant N, Delacourte A, Buee L. 2005. Tau protein as a differential biomarker of tauopathies. Biochim Biophys Acta 1739:179–197.

Sherman MY, Goldberg AL. 2001. Cellular defenses against unfolded proteins: a cell biologist thinks about neurodegenerative diseases. Neuron 29:15–32.

Shimura H, Miura-Shimura Y, Kosik KS. 2004a. Binding of tau to heat shock protein 27 leads to decreased concentration of hyperphosphorylated tau and enhanced cell survival. J Biol Chem 279:17957–17962.

Shimura H, Schwartz D, Gygi SP, Kosik KS. 2004b. CHIP-Hsc70 complex ubiquitinates phosphorylated tau and enhances cell survival. J Biol Chem 279:4869–4876.

Shin Y, Klucken J, Patterson C, Hyman BT, McLean PJ. 2005. The cochaperone carboxyl terminus of Hsp70-interacting protein (CHIP) mediates alpha-synuclein degradation decisions between proteasomal and lysosomal pathways. J Biol Chem 280:23727–23734.

Takashima A, Murayama M, Murayama O, Kohno T, Honda T, Yasutake K, Nihonmatsu N, Mercken M, Yamaguchi H, Sugihara S, Wolozin B. 1998. Presenilin 1 associates with glycogen synthase kinase-3beta and its substrate tau. Proc Natl Acad Sci U S A 95:9637–9641.

Robust estimation of the arterial input function for Logan plots using an intersectional searching algorithm and clustering in positron emission tomography for neuroreceptor imaging

Mika Naganawa,[a,b] Yuichi Kimura,[a,*] Junichi Yano,[c] Masahiro Mishina,[d] Masao Yanagisawa,[c] Kenji Ishii,[e] Keiichi Oda,[e] and Kiichi Ishiwata[e]

[a]Molecular Imaging Center, National Institute of Radiological Sciences, 4-9-1, Anagawa, Inage, Chiba-shi, Chiba, 263-8555, Japan
[b]Yale PET Center, School of Medicine, Yale University, New Haven, CT, USA
[c]Graduate School of Science and Engineering, Waseda University, Tokyo, Japan
[d]Neurological Institute, Nippon Medical School Chiba-Hokusoh Hospital, Chiba, Japan
[e]Positron Medical Center, Tokyo Metropolitan Institute of Gerontology, Tokyo, Japan

The Logan plot is a powerful algorithm used to generate binding-potential images from dynamic positron emission tomography (PET) images in neuroreceptor studies. However, it requires arterial blood sampling and metabolite correction to provide an input function, and clinically it is preferable that this need for arterial blood sampling be obviated. Estimation of the input function with metabolite correction using an intersectional searching algorithm (ISA) has been proposed. The ISA seeks the input function from the intersection between the planes spanned by measured radioactivity curves in tissue and their cumulative integrals in data space. However, the ISA is sensitive to noise included in measured curves, and it often fails to estimate the input function. In this paper, we propose a robust estimation of the cumulative integral of the plasma time–activity curve (pTAC) using ISA (robust EPISA) to overcome noise issues. The EPISA reduces noise in the measured PET data using averaging and clustering that gathers radioactivity curves with similar kinetic parameters. We confirmed that a little noise made the estimation of the input function extremely difficult in the simulation. The robust EPISA was validated by application to eight real dynamic [11C]TMSX PET data sets used to visualize adenosine A_{2A} receptors and four real dynamic [11C]PIB PET data sets used to visualize amyloid-beta plaque. Peripherally, the latter showed faster metabolism than the former. The clustering operation improved the signal-to-noise ratio for the PET data sufficiently to estimate the input function, and the calculated neuroreceptor images had a quality equivalent to that using measured pTACs after metabolite correction. Our proposed method noninvasively yields an alternative input function for Logan plots, allowing the Logan plot to be more useful in neuroreceptor studies.
© 2007 Elsevier Inc. All rights reserved.

Keywords: Positron emission tomography; Clustering; Intersectional searching algorithm; Arterial blood sampling; Logan plot

Introduction

The Logan plot (Logan et al., 1990) is a graphical approach that estimates volume of distribution (V_T) from the slope of a plot. V_T refers to the sum of the volume of distributions in the free, nonspecific binding, and specific binding compartments (Koeppe et al., 1991; Innis et al., 2007). Because this algorithm achieves more robust and faster estimation compared with nonlinear least squares methods (Carson, 2002), it is widely used for generating parametric images of V_T in neuroreceptor mapping. The Logan plot requires two measurable data sets: one is obtained by dynamic PET scanning, and the other is obtained by serial arterial blood sampling. If the serial arterial blood sampling can be omitted, the Logan plot becomes a more useful and easy-to-use approach. There are several approaches to avoiding invasive arterial blood sampling. Reference-region-based Logan plot (Logan et al., 1996) cancels out the term of the integral of the plasma time–activity curve (pTAC) using a tissue time–activity curve (tTAC) in reference regions where the target receptor is negligible. Although the term relating to the pTAC is expelled, the estimation equation still includes an efflux parameter, k_2 [1/min]. It is sometimes difficult to know the value of k_2 about reference regions in advance. If an equilibrium state is achieved between tTAC and pTAC, a priori knowledge of k_2 is not necessary, but such a

* Corresponding author.
  E-mail address: ukimura@ieee.org (Y. Kimura).
  Available online on ScienceDirect (www.sciencedirect.com).

situation is not always realized. Another approach, which we have previously proposed, is based on a statistical model: independent component analysis (Naganawa et al., 2005a,b) and variational Bayes (Naganawa et al., 2007a). These methods assume a factor analysis model in which each voxel includes the radioactivities from tissue and blood, and estimates the time–activity curve (TAC) of whole blood radioactivity. The estimated blood curve was successfully used in Logan plots as an alternative to the measured pTAC. Note that the plasma-to-whole blood ratio should be constant in the time for which the Logan plot was applied (Naganawa et al., 2005b), and the estimated blood curve includes the radioactivity in metabolites.

In applying the Logan plot, an input blood function appears in a form of the cumulative integral of the pTAC (intpTAC). It is desirable for the intpTAC to be corrected metabolically. Wang et al. proposed an intersectional searching algorithm (ISA) to estimate the intpTAC directly (Wang et al., 2005). The metabolite-corrected intpTAC will be theoretically obtained using their algorithm. However, one aspect to be considered is noise in the measured tTACs. Because of its mathematical nature, the ISA is very sensitive to noise, and it is thus important to reduce the noise effectively in estimating intpTAC. We have developed methods to reduce the measurement noise using clustering based on each TAC's kinetics (Kimura et al., 1999, 2005a,b). It is expected that our clustering method will improve estimation using ISA. In this paper, we propose a method for robust extraction of the intpTAC using ISA and clustering (robust EPISA). We clarify the sensitivity of the ISA to the measurement noise using simulations, and we investigate the applicability of the robust EPISA by applying it to dynamic PET data using [7-methyl-^{11}C]-(E)-8-(3,4,5-trimethoxystyryl)-1,3,7-tri-methylxanthine ([^{11}C]TMSX), which visualizes adenosine A_{2A} receptors (Ishiwata et al., 2000, 2005; Mishina et al., 2007), and [N-methyl-^{11}C]2-(4′-methylaminophenyl)-6-hydroxy-benzothiazole] ([^{11}C]PIB), which visualizes amyloid-beta plaque (Mathis et al., 2003; Klunk et al., 2004).

Theory

ISA

ISA (Wang et al., 2005) estimates the intpTAC using at least two tTACs with mutually different shapes and the corresponding cumulative integral of the tTACs (inttTAC) based on the equations for the Logan plot. This section provides an overview of the ISA and discusses its drawbacks. The equation for the Logan plot is described as

$$\frac{\int_0^T c^{(i)}(t)dt}{c^{(i)}(T)} = d^{(i)}\frac{\int_0^T c_p(t)dt}{c^{(i)}(T)} + b^{(i)}, \tag{1}$$

where $c^{(i)}(t)$ is a tTAC at the ith voxel or region and $c_p(t)$ is a pTAC. $\int_0^T c^{(i)}(t)dt$ and $\int_0^T c_p(t)dt$ are inttTAC at the ith voxel and intpTAC, respectively. For time $T \geq t^*$, the second term $b^{(i)}$ (<0) is a constant, and $d^{(i)}$ corresponds to a V_T. Eq. (1) is arranged for $\int_0^T c_p(t)dt$ as

$$\int_0^T c_p(t)dt = \frac{-b^{(i)}}{d^{(i)}}c^{(i)}(T) + \frac{1}{d^{(i)}}\int_0^T c^{(i)}(t)dt$$
$$= a_1^{(i)}c^{(i)}(T) + a_2^{(i)}\int_0^T c^{(i)}(t)dt. \tag{2}$$

Because the values of $d^{(i)}$ and $b^{(i)}$ are constant, constant coefficients $-b^{(i)}/d^{(i)}$ and $1/d^{(i)}$ are denoted as $a_1^{(i)}$ and $a_2^{(i)}$, respectively. Assuming that a tTAC is measured at times $T = t_1, t_2, ..., t_m$, Eq. (2) can be written in terms of vectors as

$$c_{\text{pint}} = a_1^{(i)}c^{(i)} + a_2^{(i)}c_{\text{int}}^{(i)}, \tag{3}$$

where c_{pint}, $c^{(i)}$, and $c_{\text{int}}^{(i)}$ are column vectors of m elements corresponding to $\int_0^T c_p(t)dt$, $c^{(i)}(T)$, and $\int_0^T c^{(i)}(t)dt$, respectively. Because c_{pint} is a common vector between the ith and jth voxels or regions ($i \neq j$), the following equation is obtained.

$$a_1^{(i)}c^{(i)} + a_2^{(i)}c_{\text{int}}^{(i)} = a_1^{(j)}c^{(j)} + a_2^{(j)}c_{\text{int}}^{(j)} \tag{4}$$

Eq. (4) can be rewritten as

$$(c^{(i)} \, c_{\text{int}}^{(i)} \, c^{(j)} \, c_{\text{int}}^{(j)})\begin{pmatrix} a_1^{(i)} \\ a_2^{(i)} \\ -a_1^{(j)} \\ -a_2^{(j)} \end{pmatrix} = Ca = 0, \tag{5}$$

where $C \in \mathcal{R}^{m \times 4}$ is a matrix ($m > 4$) and $a \in \mathcal{R}^{4 \times 1}$ is a column vector. Because the rank of the matrix C is at most three, the vector a can be estimated as a right singular vector corresponding to the smallest right singular value of C. Because any vector whose direction is equal to the right singular vector a satisfies Eq. (5), the length of a cannot be determined. Accordingly, the absolute value of the intpTAC cannot be determined. ISA infers only the shape of the intpTAC during the period in which the Logan plot can be applied. Although the absolute value of the V_T at each voxel cannot be determined using the Logan plot with ISA-estimated intpTAC, the ratio between them can be estimated. Note that the estimation of the intpTAC is limited to the range of time used for the Logan plot, because ISA is defined only on the frames where the Logan plot is applicable. Thus, ISA is useless in estimating the intpTAC at early times, and the estimated intpTAC cannot be used as an input function for the nonlinear least squares method.

Let us give a geometrical interpretation of ISA algorithm to allow intuitive understanding of the effect of noise. Eq. (3) means that the intpTAC vector c_{pint} is on the plane that is spanned by the tTAC vector $c^{(i)}$ and the inttTAC vector $c^{(i)}$. Eq. (4) shows that c_{pint} is an intersectional vector of two planes by the i and jth voxel. Fig. 1 shows the geometric relationship between intpTAC, the tTACs and the inttTACs. In reality, there is a large amount of noise in the measured PET data. Therefore, the plane spanned by the tTAC vector and the inttTAC vector is deviated from the true plane. Accordingly, the measurement noise produces estimation error in the direction of the intersectional vector c_{pint}.

Robust EPISA

The proposed method, robust EPISA, improves the signal-to-noise ratio of the measured PET data using averaging and clustering. The voxels that locate close to each other tend to have similar kinetics. In addition, there exist tTACs that have similar kinetics but locate at separate positions. In robust EPISA, first, a spatial averaging filter is applied. Clustering is subsequently performed to gather tTACs based on their kinetics, and tTACs classified into the same cluster are averaged. Finally,
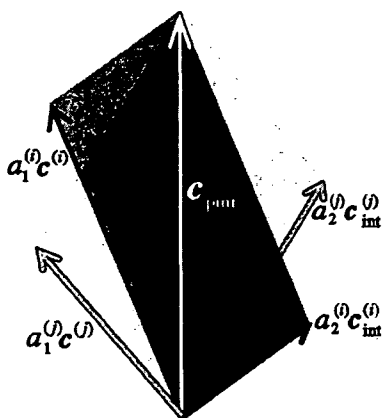
Fig. 1. Schematic illustration of a relationship between intpTAC, the tTACs, and the inttTACs. The intpTAC is estimated as an intersection vector of two planes.

the intersection-searching algorithm is applied to noise-reduced data.

To reduce noise, clustering was performed using a quantity proposed in (Kimura et al., 1999, 2002). The quantity, R, is defined as

$$R = \frac{\int_0^T c^{(i)}(t)\,dt}{\int_0^T tc^{(i)}(t)\,dt} \qquad (6)$$

where T is the time of the final frame. The amplitude of R is determined by only the shape of the tTAC emphasized by t. The quantity R is invariant when the tTAC becomes the product of a constant α times the tTAC $c^{(i)}(t)$, because α is canceled out between the numerator and the denominator in Eq. (6). Therefore, the quantity R evaluates the tTAC's shape. For example, the quantity R becomes a function of a kinetic efflux parameter k_2 when a kinetic of the administered radioligand is described by a one-tissue two-compartment model (Kimura et al., 1999).

The actual procedures in robust EPISA are shown below.

1. The region outside the brain was excluded and voxel-based PET data were spatially averaged.
2. The quantity, R, was calculated about each voxel, and voxels with similar R were categorized into one cluster. The same number of voxels were assigned to each cluster.
3. The tTACs categorized into the same cluster were averaged. Note that each tTAC was normalized by each time integral.
4. The intpTACs were estimated from all possible pairs of the averaged tTACs.
5. The candidate intpTACs were obtained from all estimated intpTACs by excluding failed curves, and the final result was the averaged candidate intpTACs.

A suitable size of clusters for Step 2 was investigated. An intpTAC should be a monotonically increasing function with positive values. The failed curves in Step 5 mean the intpTACs with negative values or the intpTACs that do not monotonically increase. In Step 5, a scale of the intpTAC should be normalized before averaging because it cannot be determined using ISA.

Materials and methods

Simulations

Simulations were carried out to investigate the behavior of the ISA in the presence of noise to make sure of the necessity of noise reduction in applying ISA. Perfect tTACs were generated using a metabolite-corrected pTAC obtained from a human [11C]TMSX study with serial arterial blood sampling. Kinetic parameter values of [11C]TMSX in the putamen and the frontal lobe (Naganawa et al., 2007b) were chosen for the generation of noise-free tTACs ($K_1 = 0.32$ (mL plasma)·min^{-1} (mL tissue)$^{-1}$, $k_2 = 0.43$ min^{-1}, $k_3 = 0.44$ min^{-1}, $k_4 = 0.36$ min^{-1} and $K_1 = 0.29$ (mL plasma)·min^{-1} (mL tissue)$^{-1}$, $k_2 = 0.39$ min^{-1}, $k_3 = 0.13$ min^{-1}, $k_4 = 0.29$ min^{-1}, respectively). Noisy data were subsequently obtained by adding Gaussian noise to the noise-free data. Added noise was expressed as $\mathcal{N}\left(0, \beta\frac{c(t)}{\Delta t}\right)$, where Δt is the frame width and β is a proportional constant that represents the noise level. The simulations were conducted for a protocol of 27 frames over a period of 1 h (10 s × 6, 30 s × 3, 60 s × 5, 150 s × 5, and 5 min × 8). The noise level β was set to be 0 and 16. The noise level was scaled so that the value of 16 corresponded to the averaged tTAC over 100 voxels. In the simulation, 20 realizations of noisy tTACs were generated, and 10 pairs of tTACs were randomly selected from the tTACs, and ISA was applied to them because an intpTAC is estimated using two tTACs in EPISA. ISA was also applied to noise-free tTACs. Because it is possible to apply Logan plots to [11C]TMSX 10 min after administration (Naganawa et al., 2007b), ISA was performed using the simulated data between 27.5 and 57.5 min after administration. The estimated intpTACs were compared with the true intpTAC.

[11C]TMSX PET studies

The presented method (robust EPISA) was applied to eight human [11C]TMSX PET data sets in order to investigate the effects of averaging and clustering. The Ethics Committee of Tokyo Metropolitan Institute of Gerontology approved the study protocol. [11C]TMSX PET data were acquired from seven healthy volunteers and one patient with Parkinson's disease. Written informed consent was obtained from all subjects before the study. After a transmission scan, 590 ± 103 MBq of [11C]TMSX with a specific activity of 40 ± 21 GBq/μmol was administered intravenously, and a 1 h dynamic PET scan was performed in two-dimensional mode using a SET-2400W (Shimadzu Co., Kyoto, Japan). The acquisition consisted of 27 frames of data (10 s × 6, 30 s × 3, 60 s × 5, 150 s × 5, and 5 min × 8). The dynamic PET data were reconstructed using a filtered back-projection algorithm with a second-order low-pass filter with a cutoff frequency of 1.25 cycles/cm. Twenty-five slices were scanned–each slice with 96 × 96 voxels–and the resulting voxel size was 2 × 2 × 6.25 mm. Serial arterial blood sampling and metabolite analysis were performed during the scan. Arterial blood samples were taken from the brachial artery at 10, 20, 30, 40, 50, 60, 70, 80, 90, 100, 110, 120, 135 and 150 s and 3, 5, 7, 10, 15, 20, 30, 40, 50 and 60 min. The radioactivity in the plasma was measured using a well-type gamma counter (BSS-1, Shimadzu Co., Kyoto, Japan) against which the PET camera was cross-calibrated. The unmetabolized fraction was measured by high-performance liquid chromatography (Ishiwata et al., 2003). The unmetabolized fraction in the plasma samples was fitted to the function proposed in Watabe et al. (2000).

Fifteen slices that cover the whole brain were used for estimation by robust EPISA. The regions outside the brain were specified as the voxels below the 70th percentile of the summed PET images and were excluded from the target of the robust EPISA. Approximately 63,000 voxels were used for the estimation. The 5-by-5 average filter was applied to the measured PET images to improve the signal-to-noise ratio by spatial averaging. The number of clusters was set to 50, and approximately 1250 voxels were included in one cluster. Thus, sufficiently noise-reduced tTACs were obtained. PET images taken between 27.5 and 57.5 min after administration were used in the ISA. The estimated intpTAC was divided by its value at the last frame for normalization. Logan plot was applied to obtain the V_T image using the metabolite-corrected intpTAC and the estimated intpTAC. The centrum semiovale was manually defined as a reference region, and the binding potential, BP_{ND}, image was given by $\dfrac{V_T}{V_{ND}} - 1$ where V_{ND} is the averaged V_T over the centrum semiovale.

[^{11}C]PIB PET studies

The peripheral metabolism of [^{11}C]TMSX is slow; more than 95% of administered [^{11}C]TMSX remains as the intact form at 60 min post injection (Naganawa et al., 2007b). Therefore, the measured pTACs with and without metabolite correction have similar shape in [^{11}C]TMSX data. In order to investigate the influence of metabolites included in plasma and the number of clusters, the robust EPISA was also applied to four human [^{11}C] PIB PET data sets with faster metabolism. Parent fraction of [^{11}C] PIB was 48±13% at 20 min and 30±8% at 60 min post injection. The Ethics Committee of Tokyo Metropolitan Institute of Gerontology approved the study protocol. [^{11}C]PIB PET data were acquired from two healthy volunteers and two patients with Alzheimer disease who met the criteria of probable AD by NINDS-ADRDA and Dementia of Alzheimer's Type with DSM-IV. Written informed consent was obtained from all subjects before the study. After a transmission scan, 455±55 MBq of [^{11}C]PIB with a specific activity of 88±32 GBq/μmol was administered intravenously, and a 1 h dynamic PET scan was performed in three-dimensional mode using the same scanner as [^{11}C]TMSX scan. The acquisition consisted of 23 frames of data (10 s×6, 20 s×3, 60 s×2, 2 min×1, 4 min×1, and 5 min×10). Image reconstruction, serial arterial blood sampling and metabolite analysis were conducted in the same way as [^{11}C]TMSX scan, and 50 slices were scanned.

Slices that cover the whole brain were used for estimation by robust EPISA. The regions outside the brain were specified as the voxels below the 80th percentile of the summed PET images and were excluded from the target of the robust EPISA. Approximately 126,000 voxels were used for the estimation. The 9-by-9 average filter was applied to the measured PET images. The number of clusters was set to 10 (12,600 voxels/cluster), 20 (6300 voxels/cluster), 40 (3150 voxels/cluster) and 80 (1575 voxels/cluster). ISA was applied to PET images taken between 37.5 and 57.5 min after administration (Price et al., 2005; Lopresti et al., 2005). The estimated intpTAC was divided by its value at the last frame for normalization. Logan plot was applied to obtain the V_T image using the metabolite-corrected intpTAC and the estimated intpTAC. The cerebellum was manually defined as a reference region (Price et al., 2005), and the distribution volume ratio (DVR) image was calculated.

Results

Simulation

The noise sensitivity of the ISA was confirmed using the simulated [^{11}C]TMSX data. The noise-free tTACs and examples of noise-added tTACs used for the simulation are presented in Fig. 2. Fig. 3 shows the estimated intpTACs and the true intpTAC. The scale was adjusted so that the value at the last frame corresponds to that of the true intpTAC. There was no difference between the ISA-estimated intpTAC and the true intpTAC with noise-free data. However, the estimated intpTACs were apparently deviated from the true intpTAC with a noise level of 16.

[^{11}C]TMSX PET studies

Clustering results are shown in Figs. 4 and 5. In Fig. 5, the voxels that have larger clustering criterion R are represented in a brighter color. While the neighboring voxels tend to belong to the same cluster and brain structure can be observed in Fig. 5, some remote voxels were also categorized into the same cluster. The intpTAC was estimated from the clustered and averaged tTACs as shown in Fig. 4. The noise level in the cluster-averaged tTACs was well suppressed. The estimated intpTACs using the proposed robust EPISA is demonstrated with standard deviation in Fig. 6(A). Note that standard deviation was not calculated from all estimated intpTACs but the candidate intpTACs as described in Step 5 in the Robust EPISA section. The estimated intpTACs were similar to the measured intpTACs with metabolite correction. The scale of the robust EPISA estimated intpTAC cannot be determined. In order to compare the estimated intpTACs with the measured intpTACs, the estimated intpTACs were scaled using the value at the last frame. The measured intpTACs without metabolite correction were also scaled using the value at the last frame. It took 5 to 7 s to estimate the intpTAC from one subject's data. The Logan plot was applied to the measured PET data to generate the V_T parametric images, and Fig. 7 shows BP_{ND} images calculated using the estimated V_T
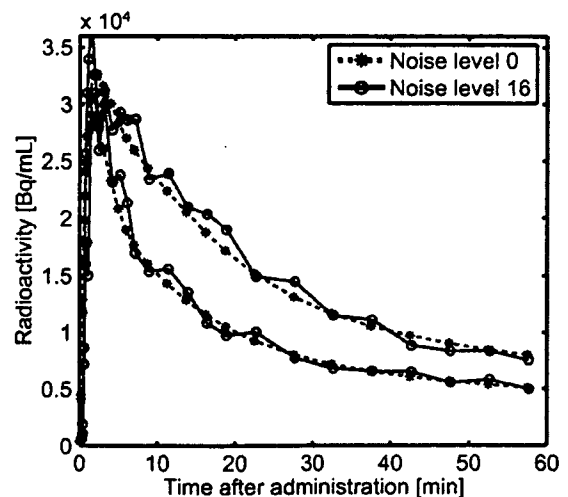

Fig. 2. Example of noise-free tTACs (dashed lines) and noisy tTACs (solid lines) for the simulation investigating the influence of noise in tTACs. The noise level of the noisy tTACs was set to 16. Two kinds of tTACs were used for estimation using ISA.
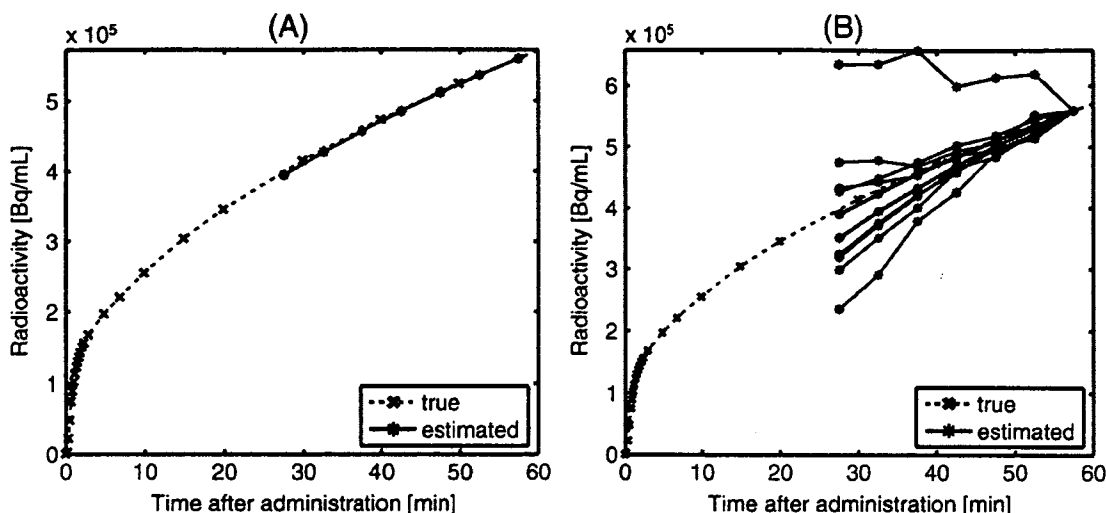
Fig. 3. Estimated intpTACs from the noise-free data (A) and the noisy data (B). The period used for the ISA was 27.5 min to 57.5 min after administration. The true intpTAC was obtained by cumulatively integrating the true pTAC. The estimated intpTACs are shown as solid lines, and the true intpTACs are shown as dashed lines. The scale of the estimated intpTAC was adjusted using the value at the last frame.

parametric images and the specified reference region. The BP_{ND} images with the estimated and measured intpTACs matched well in all eight subjects. In the linear regression between the measured and estimated BP_{ND} images, the slopes and y-intercepts were 1.00 ± 0.011 and 0.035 ± 0.016, respectively. The coefficient of determination (r^2) was 1.00 ± 0.0016.

[^{11}C]PIB PET studies

Fig. 6(B) shows the estimated intpTAC and the standard deviation calculated from candidate intpTACs. The estimated intpTACs were similar to the measured intpTACs with metabolite correction. For comparison, the scale of the estimated intpTACs and the measured intpTACs without metabolite correction was adjusted using the value at the last frame of the measured intpTACs
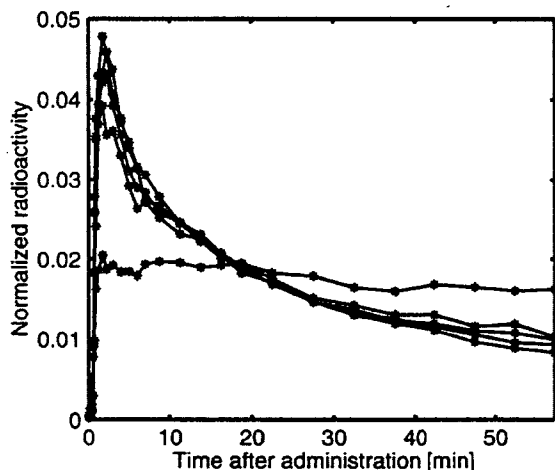

Fig. 4. Representative tTACs after clustering in [^{11}C]TMSX data. The tTACs of the measured PET data were categorized into 50 clusters and subsequently averaged in each cluster. Each tTAC was normalized by dividing by its integral.

with metabolite correction. The calculation time was comparable to [^{11}C]TMSX study. The relationship between the number of clusters and estimation results were demonstrated in Fig. 8. Standard deviation increased as the size of the clusters became smaller. However, the final estimated intpTAC was little influenced by the choice of the number of clusters. In each case with different number of clusters, the candidate intpTACs from which the final result was obtained were approximately 22% curves out of all estimated intpTACs. When the number of the clusters set to be less than 5, the proposed method did not work. The Logan plot was applied to the measured PET data to generate the V_T parametric images, and Fig. 9 shows the DVR images of Alzheimer disease patient that were calculated using the estimated V_T parametric images in case of 20 clusters. The DVR images with the estimated and measured intpTACs matched well in all four subjects. In the linear regression between the measured and estimated DVR images, the slopes and y-intercepts were 0.97 ± 0.038 and 0.060 ± 0.057, respectively. The coefficient of determination (r^2) was 0.97 ± 0.026.

Discussion

The proposed method, robust EPISA, settles the mathematical drawback in ISA, in that performance is influenced by the noise in the measured tTACs. The measurement noise included in PET data was reduced by clustering based on tTAC's kinetics, and an input function for Logan plots was estimated robustly based on ISA (Wang et al., 2005). Robust EPISA estimates a shape of a cumulative integral curve of pTAC appearing in the operational equation of the Logan plot, and enables binding-potential imaging to be generated with no arterial blood sampling or metabolite correction. Omission of arterial blood sampling reduces the invasiveness of PET measurement and contributes to the shortened total time needed for preparation of serial arterial blood sampling. Before discussing the robustness of the proposed method, we should consider the advantages and disadvantages of ISA.

ISA has two advantages: no requirement for metabolite correction of pTAC and wide applicability to PET data with various radioligands, because of the broad application of the Logan
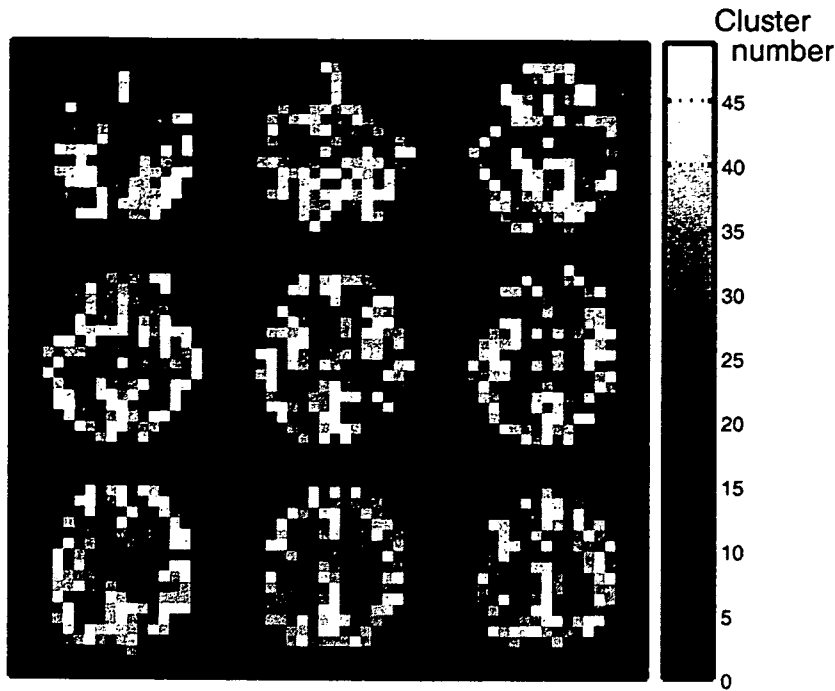
Fig. 5. Example of a clustered image in [^{11}C]TMSX data. The voxel value corresponds to the cluster number. As the cluster number becomes larger, the corresponding criterion R also becomes larger.

plot. Many methods have been proposed to preclude arterial blood sampling. One of these methods is based on a factor model to estimate the shape of a whole blood curve (Barber, 1980; Paola et al., 1982; Wu et al., 1995; Lee et al., 2001; Naganawa et al., 2005a,b), where the radioactivity in the measured PET data is assumed to be the sum of the radioactivities in the blood and tissue. In this method, metabolite correction is unattainable. On the other hand, ISA can theoretically give a metabolite-corrected pTAC. ISA is derived from the operational equation for the Logan plot, and the

equations of the Logan plot are based on a compartment model. Thus, the estimated intpTAC does not include the radioactivity in metabolites. There is a great difference between the measured intpTAC with and without metabolite correction in [^{11}C]PIB data. The estimated intpTAC matched well with the measured intpTAC with metabolite correction as shown in Fig. 6. From our results, the estimated BP$_{ND}$ of [^{11}C]TMSX (Fig. 7) or DVR of [^{11}C]PIB (Fig. 9) using the proposed method coincide well with those using a measured pTAC with metabolite correction. It is expected that ISA

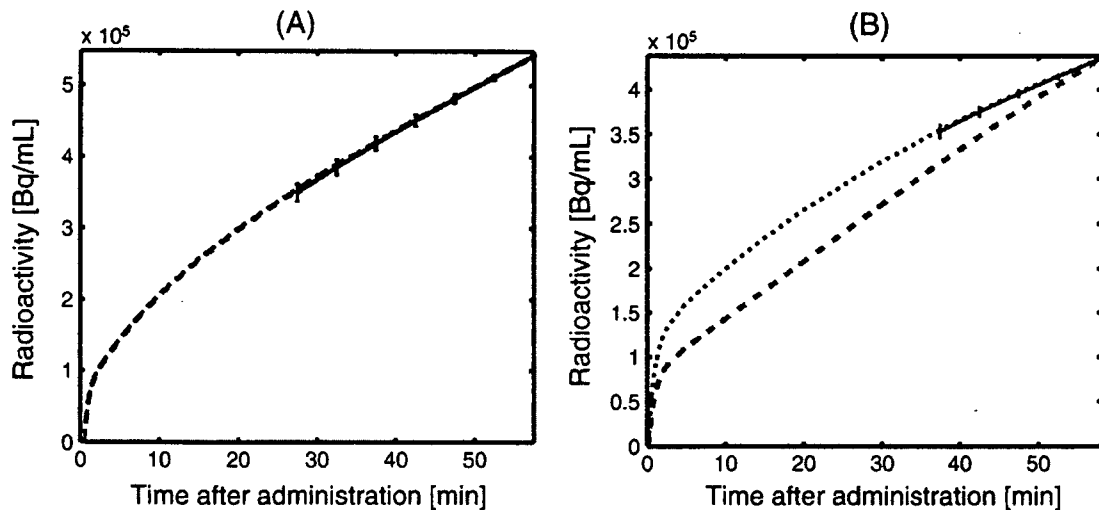Fig. 6. Example of a robust EPISA-estimated intpTAC (black solid line) in (A) [^{11}C]TMSX and (B) [^{11}C]PIB. In [^{11}C] PIB, 40 clusters were used for clustering. Measured intpTACs with and without metabolite correction were plotted in black dotted line and gray break line, respectively. Standard deviation was calculated from the candidate intpTACs.

will be applicable to radiopharmaceuticals whose metabolites cannot be ignored, or PET data with metabolism varied because of disease, dose, or other pathophysiological situations.

The next issue is the wide applicability of ISA. Using ISA, parametric images of BP_{ND} can be calculated using the estimated intpTAC and the specified reference region. When arterial blood sampling is not available, the basis function method (Gunn et al., 1997) is commonly used. While the basis function method is appropriate only when the PET data is described by a simplified reference tissue model (Lammertsma and Hume, 1996), ISA can be applied to any PET data with reversibly binding tracers. In this paper, to assure the wide applicability, EPISA was applied to two radioligands: [^{11}C]TMSX with slow peripheral metabolism and [^{11}C]PIB with fast one.

ISA has a disadvantage in practical application because of its high sensitivity to measurement noise. ISA is an algorithm to estimate the intersection between the planes spanned by tTAC and inttTAC. As shown in Fig. 3, ISA failed in estimating the intpTAC, even with low-noise. The reason for this is considered here. The ISA algorithm leads to the singular value decomposition problem. Generally, the singular vector with the smallest singular value is inaccurately estimated in the presence of noise. Therefore, it is important to reduce noise from the measured PET data before applying ISA.

In addition, the absolute value of the intpTAC cannot be estimated using ISA, as with other mathematical algorithms for the pTAC estimation (Barber, 1980; Paola et al., 1982; Wu et al., 1995; Lee et al., 2001; Naganawa et al., 2005a,b), because only the direction of a singular vector is presumable. Therefore, the relative V_T is obtained using Logan plot with the estimated pTAC or intpTAC. At least one-point arterial blood sampling is required to scale the estimated pTAC or intpTAC and calculate the absolute V_T. However, BP_{ND} can be calculated from the ratio of V_T values between target voxels and the reference region, and this calculation does not require the absolute value of the intpTAC. ISA can form the parametric image of BP_{ND} by specifying reference region.

In this study, a kinetic model-based clustering scheme was applied for noise reduction. It has been successfully applied in the rapid and robust parametric imaging of regional cerebral blood flow (Kimura et al., 1999) and [^{18}F]FDG studies (Kimura et al., 2002). In this paper, we proposed averaging and clustering as a way to successful ISA. The measured tTACs were clustered based on their kinetic shape. In the [^{11}C]TMSX studies, approximately 1250 voxels were assigned to a single cluster. Although the size of the cluster is too large as an anatomical ROI, such a large ROI is appropriate for EPISA because reducing noise is more important than increasing heterogeneity in the clusters. The estimated result was not influenced too much by the choice of the number of the clusters as shown in Fig. 8. IntpTACs were estimated from all possible pairs of the noise-reduced tTACs. In some pairs, estimated intpTACs were not monotonically increasing. The derivative of the intpTAC equals the pTAC. Therefore, the pTAC includes negative values when the intpTAC was not monotonically increasing.

The reference-region-based Logan plot also successfully estimates DVR or BP_{ND} without arterial blood sampling. Comparing EPISA with the reference-region-based Logan plot, robust EPISA does not need any kinetic parameters, while the reference-region-based Logan plot requires the population value of k_2 in the reference region in advance. We think that it is an advantage over the noninvasive Logan analysis. Note that noninvasive Logan analysis

and our method will provide comparable results when the values of k_2 in a reference region are sufficiently similar in all subjects.

Exact values should be specified for the set of parameters used in the robust EPISA: the size of the averaging filter and the number of clusters. When the PET data have a low signal-to-noise ratio, a larger averaging filter and fewer clusters are preferable. We conclude that the ISA is a practical algorithm for the obviation of arterial blood sampling using noise reduction with clustering.

Acknowledgments

References

Barber, D.C., 1980. The use of principal components in the quantitative analysis of gamma camera dynamic studies. Phys. Med. Biol. 25 (2), 283–292.

Carson, R.E., 2002. Positron Emission Tomography Basic Science and Clinical Practice. Springer, Ch. 6, pp. 147–179.

Gunn, R.N., Lammertsma, A.A., Hume, S.P., Cunningham, V.J., 1997. Parametric imaging of ligand–receptor in PET using a simplified reference region model. NeuroImage 6 (4), 279–287.

Innis, R.B., Cunningham, V.J., Delforge, J., Fujita, M., Gjedde, A., Gunn, R.N., Holden, J., Houle, S., Huang, S.-C., Ichise, M., Iida, H., Ito, H., Kimura, Y., Koeppe, R.A., Knudsen, G.M., Knuuti, J., Lammertsma, A.A., Laruelle, M., Logan, J., Maguire, R.P., Mintun, M.A., Morris, E.D., Parsey, R., Price, J.C., Slifstein, M., Sossi, V., Suhara, T., Votaw, J.R., Wong, D.F., Carson, R.E., 2007. Consensus nomenclature for in vivo imaging of reversibly binding radioligands. J. Cereb. Blood Flow Metab. 27 (9), 1533–1539.

Ishiwata, K., Ogi, N., Shimada, J., Nonaka, H., Tanaka, A., Suzuki, F., Senda, M., 2000. Further characterization of a CNS adenosine A_{2a} receptor ligand [^{11}C]KF18446 with in vitro autoradiography and in vivo tissue uptake. Ann. Nucl. Med. 14 (2), 81–89.

Ishiwata, K., Wang, W.-F., Kimura, Y., Kawamura, K., Ishii, K., 2003. Preclinical studies on [^{11}C]TMSX for mapping adenosine A_{2A} receptors by positron emission tomography. Ann. Nucl. Med. 17 (3), 205–211.

Ishiwata, K., Mishina, M., Kimura, Y., Oda, K., Sasaki, T., Ishii, K., 2005. First visualization of adenosine A_{2A} receptors in the human brain by positron emission tomography with [^{11}C]TMSX. Synapse 55 (2), 133–136.

Kimura, Y., Hsu, H., Toyama, H., Senda, M., Alpert, N.M., 1999. Improved signal-to-noise ratio in parametric images by cluster analysis. Neuro-Image 9 (5), 554–561.

Kimura, Y., Senda, M., Alpert, N.M., 2002. Fast formation of statistically reliable FDG parametric images based on clustering and principal components. Phys. Med. Biol. 47 (3), 455–468.

Kimura, Y., Naganawa, M., Yano, J., 2005a. Multidimensional clustering for molecular imaging using positron emission tomography and Logan plot to improve noise reduction capability. Proceedings of the International Federation for Medical and Biological Engineering, vol. 12, p. 2A2-01. Singapore.

Kimura, Y., Yano, J., Tsukahara, M., Naganawa, M., Ishii, K., Ishiwata, K., 2005b. Clustering approach for voxel-based Logan plot to improve noise reduction capability. VIIth International Conference on Quantification of Brain Function with PET. Amsterdam, Netherlands, p. S632.

Klunk, W.E., Engler, H., Nordberg, A., Wang, Y., Blomqvist, G., Holt, D.P., Bergström, M., Savitcheva, I., Huang, G.-F., Estrada, S., Ausén, B., Debnath, M.L., Barletta, J., Price, J.C., Sandell, J., Lopresti, B.J., Wall, A., Koivisto, P., Antoni, G., Mathis, C.A., Långström, B., 2004. Imaging brain amyloid in Alzheimer's disease with Pittsburgh Compound-B. Ann. Neurol. 55 (3), 306–319.

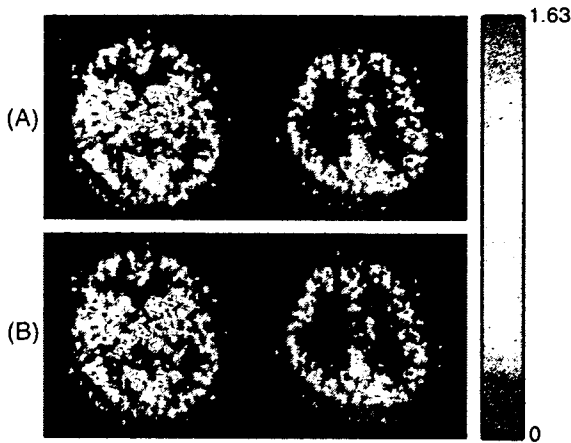Koeppe, R.A., Holthoff, V.A., Frey, K.A., Kilbourn, M.R., Kuhl, D.E., 1991.

Fig. 7. Example of the parametric images of the BP_{ND} in [^{11}C]TMSX PET data using the robust EPISA-estimated intpTAC (A) and the measured intpTAC with metabolite correction (B). These images were calculated from the V_T images and a reference region.
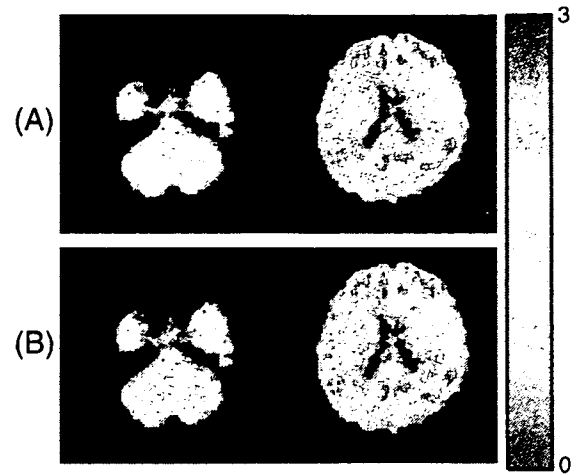

Fig. 9. Example of the parametric images of [^{11}C]PIB DVR in brain with Alzheimer disease. These images were calculated from the V_T images and a reference region using the robust EPISA-estimated intpTAC (A) and the measured intpTAC with metabolite correction (B).
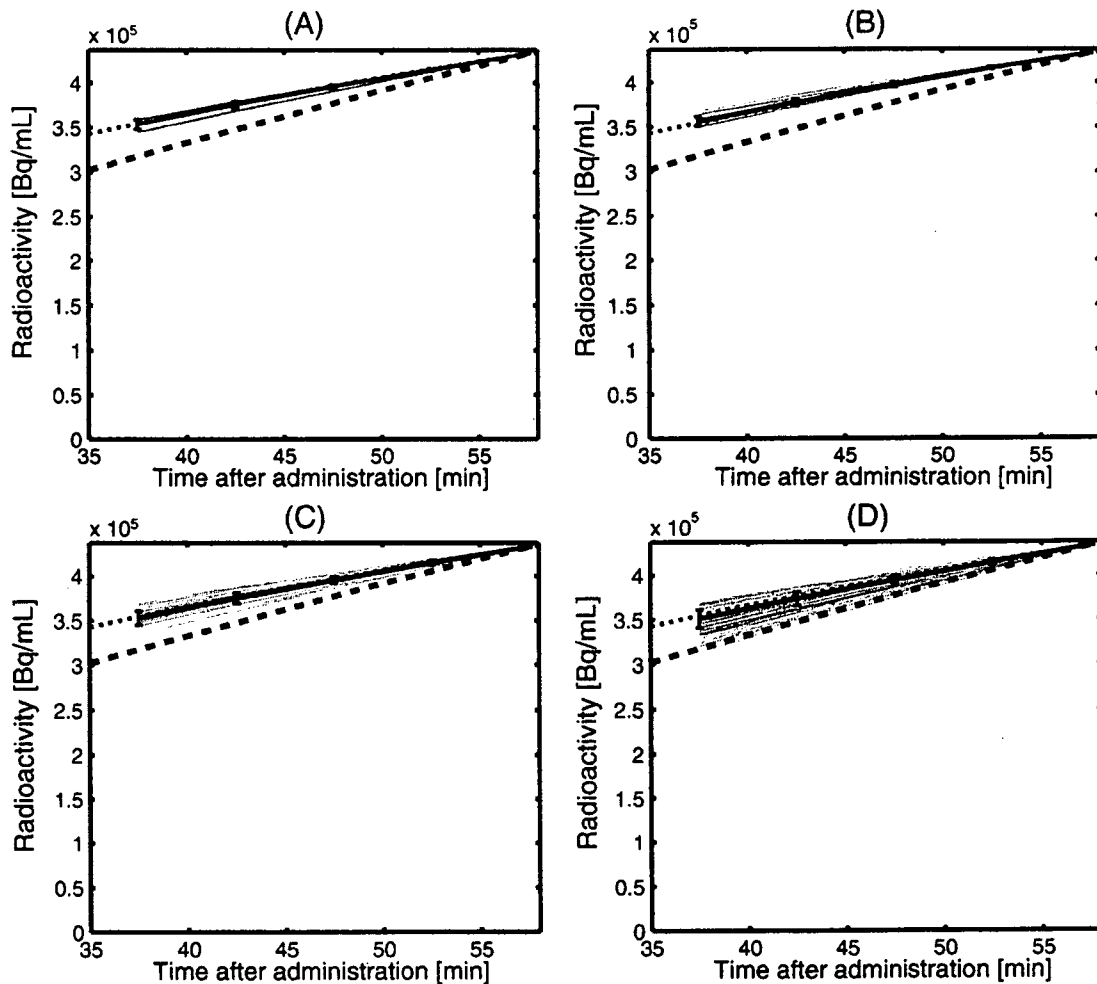

Fig. 8. Typical example of robust EPISA-estimated intpTACs (black solid line) in [^{11}C]PIB. The number of clusters was set to (A) 10, (B) 20, (C) 40, and (D) 80. Measured intpTACs with and without metabolite correction were plotted in black dotted line and gray break line. Standard deviation was calculated from the candidate intpTACs that were shown in gray solid lines.

Compartmental analysis of [^{11}C]flumazenil kinetics for the estimation of ligand transport rate and receptor distribution using positron emission tomography. J. Cereb. Blood Flow Metab. 11 (5), 735–744.

Lammertsma, A.A., Hume, S.P., 1996. Simplified reference tissue model for PET receptor studies. NeuroImage 4, 153–158.

Lee, J.S., Lee, D.S., Ahn, J.Y., Cheon, G.J., Kim, S.K., Yeo, J.S., Seo, K., Park, K.S., Chung, J.K., Lee, M.C., 2001. Blind separation of cardiac components and extraction of input function from H$_2$^{15}O dynamic myocardial PET using independent component analysis. J. Nucl. Med. 42 (6), 938–943.

Logan, J., Fowler, J.S., Volkow, N.D., Wolf, A.P., Dewey, A.L., Schlyer, D.J., MacGregor, R.R., Hitzeman, R., Bendriem, B., Gatley, S.J., Christman, D.R., 1990. Graphical analysis of reversible radioligand binding from time–activity measurements applied to [n-^{11}C-methyl]-(−)-cocaine PET studies in human subjects. J. Cereb. Blood Flow Metab. 10 (5), 740–747.

Logan, J., Fowler, J.S., Volkow, N.D., Wang, G.-J., Ding, Y.-S., Alexoff, D.L., 1996. Distribution volume ratios without blood sampling from graphical analysis of PET data. J. Cereb. Blood Flow Metab. 16 (5), 834–840.

Lopresti, B.J., Klunk, W.E., Mathis, C.A., Hoge, J.A., Ziolko, S.K., Lu, X., Meltzer, C.C., Schimmerl, K., Tsopelas, N.D., DeKosky, S.T., Price, J.C., 2005. Simplified quantification of Pittsburgh Compound B amyloid imaging PET studies: a comparative analysis. J. Nucl. Med. 46 (12), 1959–1972.

Mathis, C.A., Wang, Y., Holt, D.P., Huang, G.-F., Debnath, M.L., Klunk, W.E., 2003. Synthesis and evaluation of ^{11}C-labeled 6-substituted 2-arylbenzothiazoles as amyloid imaging agents. J. Med. Chem. 46 (13), 2740–2754.

Mishina, M., Ishiwata, K., Kimura, Y., Naganawa, M., Oda, K., Kobayashi, S., Katayama, Y., Ishii, K., 2007. Evaluation of distribution of adenosine A$_{2A}$ receptors in normal human brain measured with [^{11}C]TMSX PET. Synapse 61 (9), 778–784.

Naganawa, M., Kimura, Y., Ishii, K., Oda, K., Ishiwata, K., Matani, A., 2005a. Extraction of a plasma time–activity curve from dynamic brain

PET images based on independent component analysis. IEEE Trans. Biomed. Eng. 52 (2), 201–210.

Naganawa, M., Kimura, Y., Nariai, T., Ishii, K., Oda, K., Manabe, Y., Chihara, K., Ishiwata, K., 2005b. Omission of serial arterial blood sampling in neuroreceptor imaging with independent component analysis. NeuroImage 26 (3), 885–890.

Naganawa, M., Kimura, Y., Ishii, K., Oda, K., Ishiwata, K., 2007a. Temporal and spatial blood information estimation using Bayesian ICA in dynamic cerebral positron emission tomography. Digit. Signal Process. 17 (5), 979–993.

Naganawa, M., Kimura, Y., Mishina, M., Manabe, Y., Chihara, K., Oda, K., Ishii, K., Ishiwata, K., 2007b. Quantification of adenosine A$_{2A}$ receptors in the human brain using [^{11}C]TMSX and positron emission tomography. Eur. J. Nucl. Med. Mol. Imaging 34 (5), 679–687.

Di Paola, R., Bazin, J.P., Aubry, F., Aurengo, A., Cavailloles, F., Herry, J.Y., Kahn, E., 1982. Handling of dynamic sequences in nuclear medicine. IEEE Trans. Nucl. Sci. NS-29 (4), 1310–1321.

Price, J.C., Klunk, W.E., Lopresti, B.J., Lu, X., Hoge, J.A., Ziolko, S.K., Holt, D.P., Meltzer, C.C., DeKosky, S.T., Mathis, C.A., 2005. Kinetic modeling of amyloid binding in humans using PET imaging and Pittsburgh Compound-B. J. Cereb. Blood Flow Metab. 25 (11), 1528–1547.

Wang, Z.J., Peng, Q., Liu, K.J.R., Szabo, Z., 2005. Model-based receptor quantization analysis for PET parametric imaging. 27th Annual International Conference of the IEEE Engineering in Medicine and Biology Society, pp. 5908–5911.

Watabe, H., Channing, M.A., Der, M.G., Adams, H.R., Jagoda, E., Herscovitch, P., Eckelman, W.C., Carson, R.E., 2000. Kinetic analysis of the 5-HT$_{2A}$ ligand [^{11}C]MDL 100,907. J. Cereb. Blood Flow Metab. 20, 899–909.

Wu, H.M., Hoh, C.K., Choi, Y., Schelbert, H.R., Hawkins, R.A., Phelps, M.E., Huang, S.C., 1995. Factor analysis for extraction of blood time–activity curves in dynamic FDG-PET studies. J. Nucl. Med. 36 (9), 1714–1722.

Presynaptic and postsynaptic nigrostriatal dopaminergic functions in multiple system atrophy

Masaya Hashimoto[a,c], Keiichi Kawasaki[a], Masahiko Suzuki[a,c], Kazuko Mitani[a,d], Shigeo Murayama[b], Masahiro Mishina[a,e], Keiichi Oda[a], Yuichi Kimura[a], Kiichi Ishiwata[a], Kenji Ishii[a] and Kiyoharu Inoue[c]

[a]Positron Medical Center, [b]Department of Neuropathology, Tokyo Metropolitan Institute of Gerontology, [c]Department of Neurology, Jikei University School of Medicine, [d]Department of Neurology, Tokyo Metropolitan Geriatric Hospital, Tokyo and [e]Neurological Institute, Nippon Medical School Chiba Hokusoh Hospital, Chiba, Japan

Correspondence to Kenji Ishii, Positron Medical Center, Tokyo Metropolitan Institute of Gerontology, 1-1 Naka-cho, Itabashi-ku, Tokyo 173-0022, Japan
Tel: +81 3 3964 3241 EX3503; fax: +81 3 3964 2188; e-mail: ishii@pet.tmig.or.jp

A simultaneous evaluation of presynaptic and postsynaptic dopaminergic positron emission tomography markers, the dopamine transporters and the dopamine D_2-like receptors, was performed in eight patients with parkinsonian phenotype of multiple system atrophy. Both presynaptic and postsynaptic markers were revealed to have declined in such a manner that they kept strong positive correlation throughout the striatum of all patients, suggesting that the degeneration process in the striatum may involve the entire structure of the dopaminergic synapse. In two L-3,4,dihydroxyphenyl-alanine-responsive cases, the balance of decline in two markers was relatively shifted to presynaptic dominant side. Correlative positron emission tomography study of presynaptic and postsynaptic dopaminergic function may be useful for the diagnosis of multiple system atrophy and to understand the mechanisms of its temporal L-3,4,dihydroxyphenyl-alanine responsiveness. NeuroReport 19:145–150 © 2008 Wolters Kluwer Health | Lippincott Williams & Wilkins.

Keywords: dopamine receptor, dopamine transporter, L-3,4,dihydroxyphenyl-alanine responsiveness, multiple system atrophy, Parkinson, positron emission tomography

Introduction

In patients with the parkinsonian phenotype of multiple system atrophy (MSA-P), a pathological abnormality is observed mainly in the substantia nigra (SN), striatum, ceruleus nucleus, pontine nuclei, inferior olivary nucleus, cerebellum, and spinal cord. The impairment is particularly severe in the SN and striatum [1], and neuronal loss and gliosis are the features of the pathology [2]. Neuroimaging studies using positron emission tomography (PET) [3] and single photon emission computed tomography techniques [4] have reported reduced glucose metabolism in the striatum and declined nigrostriatal dopaminergic neural transmission function in both the presynaptic and postsynaptic sites. No pathological or neuroimaging studies, however, have examined the relationship between the degeneration/dysfunction of nigrostriatal presynaptic and postsynaptic dopaminergic systems. It is well known that responses to L-3,4,dihydroxyphenyl-alanine (L-DOPA) are generally poor in MSA [1], and this is ascribable to the fact that the pathology of MSA involves not only SN but also the striatum where the dopamine receptors exist. A transient effect, however, is occasionally noted in the early stages in certain cases. Wenning et al. [5] proposed a hypothesis based on the pathological finding of a dissociation between the SN and striatal degeneration that may account for such L-DOPA responsiveness. No pathological or neuroimaging evidence that directly demonstrated the dissociation in such cases, however, has been found.

We simultaneously measured the presynaptic and postsynaptic nigrostriatal dopaminergic functions using PET in MSA-P patients, including L-DOPA-responsive cases, and the regional correlation of two parameters was analyzed in the striatum to examine the characteristics of the disease and the mechanisms of L-DOPA responsiveness.

Methods

This study was approved by the Ethical Committee of Tokyo Metropolitan Institute of Gerontology. The objective and effect of the PET examination on the human body were adequately explained to all participants, and written informed consent was obtained.

Participants

We studied eight patients (68.9±7.4 years old) clinically diagnosed as MSA-P according to the consensus criteria established by Gilman et al. [6] (Table 1). The MSA-P patients underwent PET examination following a 15-h deprivation of antiparkinsonian drugs. The primary symptom observed in all the patients was parkinsonism; further, during the course of the disease, parkinsonism was noted to be the cardinal symptom. Magnetic resonance imaging (MRI) examination was also performed. The characteristics of the patients are presented in Table 1. Among the eight cases of MSA-P, cases 1 and 2 apparently responded to L-DOPA at the time of the PET study, and the improvement

Table I   Clinical features of the eight patients with the parkinsonian phenotype of multiple system atrophy

Patient no./age (years)/sex	Hoehn and Yahr stage	Disease duration (years)	Autonomic dysfunction	Cerebellar dysfunction	Pyramidal sign	MRI findings	L-DOPA response
1/79/Female	III	1	+	+	+	Put	+
2/73/Female	III	1	+	+	+	Put	+
3/66/Female	I	2	+	+	+	No findings	−
4/61/Female	IV	2	+	+	+	cbll/put	−
5/72/Male	V	3	+	−	+	Put	−
6/56/Male	IV	4	+	+	+	Pons/cbll/put	−
7/73/Female	III	6	+	+	+	Pons/cbll/put	−
8/71/Female	V	9	+	−	+	Put	−

Signal change in the pons/middle cerebellar peduncles includes pontine/cerebellar atrophy (pons/cbll); Slit-like signal change at the posterolateral putaminal margin includes putaminal atrophy (put). L-DOPA, L-3,4,dihydroxyphenyl-alanine.

in the symptoms of parkinsonism due to L-DOPA was confirmed by neurologists.

The healthy control group consisted of eight participants (five men and three women, 62.3 ± 6.9 years old) that did not have a past medical history of neurological and psychiatric disorders. They were diagnosed as normal after physical and neurological examinations, screening MRI scans, and Mini-Mental Scale Evaluation (>28). They had not taken any neuroleptic drugs and were not addicted to alcohol; no history of any other substance abuse was present.

Positron emission tomography scans

^{11}C-labeled 2β-carbomethoxy-3β-(4-fluorophenyl)-tropane ([^{11}C]CFT) as a marker of presynaptic dopaminergic function for dopamine transporters and ^{11}C-labeled raclopride ([^{11}C]RAC) as a marker of postsynaptic dopaminergic function for dopamine D_2-like receptors were used as tracers for PET [7,8]. The methods used for the preparation of the radiopharmaceuticals were as described previously [9,10].

All the participants underwent the two PET studies on the same day with a 3–4-h interval. PET images were acquired in three-dimensional mode using the SET-2400W (Shimadzu, Kyoto, Japan) scanner [11] at the Positron Medical Center, Tokyo Metropolitan Institute of Gerontology. The acquired PET images were 128 × 128 × 50 in matrix size with a 2 × 2 × 3.125-mm voxel size. In PET acquisition, 300 MBq each of [^{11}C]CFT and [^{11}C]RAC were administered by an intravenous bolus injection, and all participants rested in a supine position with their eyes open during the test. The specific activity and the amount of cold material injected were 5.4–47 MBq/nM and 1.2–8.6 nM, respectively, for [^{11}C]CFT and 10–130 MBq/nM and 0.42–3.1 nM, respectively, for [^{11}C]RAC. For three of the eight healthy control participants, a dynamic scan was performed for 90 min for the [^{11}C]CFT study in the morning and for 60 min for the [^{11}C]RAC study in the afternoon to estimate the binding potentials. To measure the uptakes of these two tracers, for the five healthy participants and all the patients, a static scan was performed 75–90 min after the injection of the [^{11}C]CFT and 40–55 min after the injection of [^{11}C]RAC, respectively. The attenuation was corrected by a transmission scan using a ^{68}Ga/^{68}Ge source.

Data analysis

The two PET images of the [^{11}C]CFT and [^{11}C]RAC examinations obtained from the same participant were coregistered using an automated image registration pro-

gram [12]. The images were processed further using Dr View software (AJS, Tokyo, Japan) on Linux workstations. Next, the images were resliced in the transaxial direction parallel to the anterior–posterior intercommissural (AC-PC) line, and the regions of interest (ROIs) were placed on the three subregions of the striatum – the bilateral caudate nuclei, anterior putamen, and posterior putamen – in two slices, that is, the AC-PC plane and 3.1 mm above the AC-PC line. ROIs of the striatum consisted of circles of 8-mm diameter. On each side of each slice, we set one ROI in the caudate and two ROIs each in the anterior and posterior putamen. The reference regions of the occipital lobe were placed in four slices in a range of 12.5–21.9 mm above the AC-PC plane. The reference region of the occipital lobe consisted of circles of 10-mm diameter, and we set four such circles on each side of each slice.

First, for dynamic scan data, the binding potential of the tracer in the bilateral caudate nuclei, anterior putamen, and posterior putamen of three healthy participants was estimated by a simplified reference region model [13] using the occipital lobe as a reference. Second, for static imaging, the uptake ratio index (URI) was calculated for all participants by the following formula:

$$URI = \left(Activity_{Striatum\ subregion} - Activity_{Occipital\ lobe} \right) / Activity_{Occipital\ lobe}$$

URI was also calculated for the dynamic scan in the three healthy control participants using the data obtained from an equivalent time-frame. The URI in each ROI was compared between MSA-P patients and control participants with the Mann–Whitney U-test with Bonferroni's correction for multiple comparisons.

Next, we examined the correlation between the binding potential and the URI.

Results

For each tracer, the URIs of the striatal subregions in the static image were linearly correlated with the binding potentials in the dynamic scan ($r^2 = 0.92$, $P < 0.0001$ for [^{11}C]CFT and $r^2 = 0.93$, $P < 0.0001$ for [^{11}C]RAC). Therefore, we adopt the URI in reference to the occipital cortex for the further analysis.

Figure 1 demonstrates the representative PET images of a normal participant and an MSA-P patient. In the MSA-P patient, the URIs of both [^{11}C]CFT and [^{11}C]RAC declined in the striatum compared with the normal participant (Fig. 1).
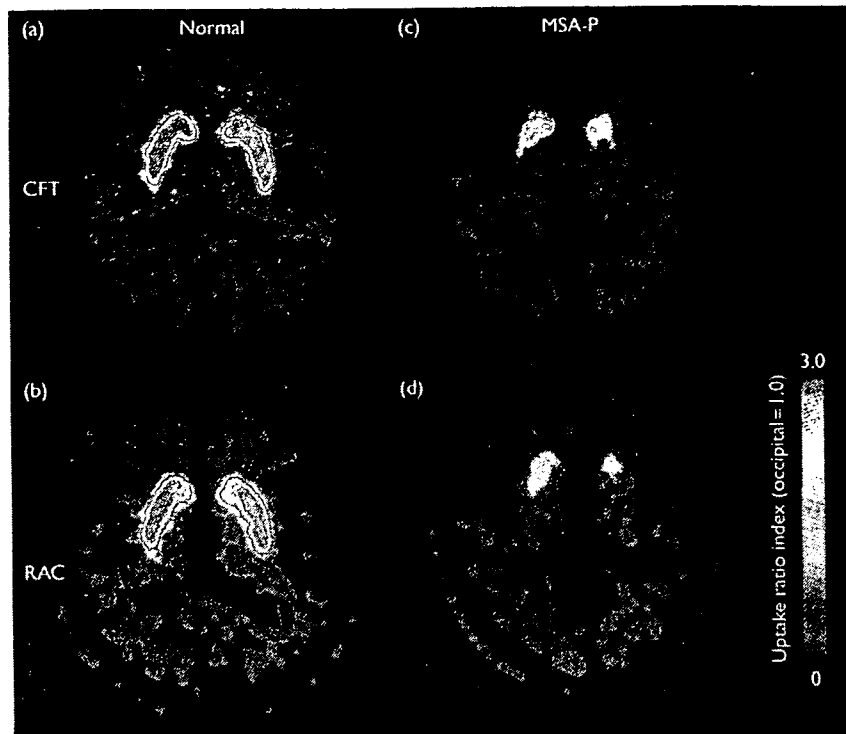
— 188 —

Fig. I Positron emission tomography images. (a) [^{11}C]CFT and (b) [^{11}C]RAC images were obtained from a normal participant, and (c) [^{11}C]CFT and (d) [^{11}C]RAC images were obtained from an MSA-P patient. All the images were normalized to the occipital lobe activity and obtained in a +3.I-mm plane from the anterior–posterior intercommissural line. [^{11}C]CFT, ^{11}C-labeled 2β-carbomethoxy-3β-(4-fluorophenyl)-tropane; [^{11}C]RAC, ^{11}C-labeled raclopride; MSA-P, phenotype of multiple system atrophy.

Table 2 The uptake ratio index of [^{11}C]CFT and [^{11}C]RAC in the subregions of the striatum

	Normal participants (n=8)	MSA-P patients (n=8)	Percentage of control
Caudate			
[^{11}C]CFT	3.70±0.55	2.49±0.41*	67.3
[^{11}C]RAC	3.46±0.40	2.63±0.31*	76.0
Anterior putamen			
[^{11}C]CFT	4.04±0.45	1.97±0.45*	48.8
[^{11}C]RAC	3.97±0.31	2.46±0.46*	62.0
Posterior putamen			
[^{11}C]CFT	3.82±0.47	1.58±0.42*	41.4
[^{11}C]RAC	3.90±0.32	2.07±0.67*	53.I

*$P<0.05$ as compared with normal controls (Mann–Whitney U-test with Bonferroni's multiple comparison correction).
[^{11}C]CFT, ^{11}C-labeled 2β-carbomethoxy-3β-(4-fluorophenyl)-tropane; [^{11}C]RAC, ^{11}C-labeled raclopride; MSA-P, phenotype of multiple system atrophy.

The results of ROI measurement are summarized in Table 2. In the MSA-P group, the URIs of both [^{11}C]CFT and [^{11}C]RAC significantly decreased in all the subdivisions of the striatum ($P<0.05$) in comparison with the control group, and the decrease was most prominent in the posterior putamen and relatively smaller in the caudate nuclei.

Scatter plots of the entire uptake data in individual participants for each of the three regions are shown in Fig. 2a–c and those for all areas are shown in Fig. 2d. A strong positive correlation was noted between the URIs of [^{11}C]CFT and [^{11}C]RAC in the MSA-P group. That is, the

impairment of presynaptic and postsynaptic nigrostriatal dopaminergic function was observed in associative degree in all the subregions of the striatum.

Two patients apparently responded to the L-DOPA administration at the time of PET studies. Figure 2 indicates that the decrease in the [^{11}C]RAC uptake was relatively lesser in comparison with that in the [^{11}C]CFT uptake in the L-DOPA-responsive cases.

Discussion

In earlier studies, the cerebellum has been widely used as a reference region to estimate the availability of dopamine transporters using [^{11}C]CFT [14,15] and dopamine D$_2$-like receptors using [^{11}C]RAC [16]. We, however, selected the occipital cortex as a reference region in this study. Neuropharmacological evidence has revealed that the densities of both the dopamine transporters and dopamine D$_2$-like receptors in the human occipital cortex are negligible as in the case of the cerebellum [17]. Furthermore, the cerebellum is often involved in the pathological processes in MSA-P, whereas the occipital lobe is less likely to be affected. The selection of the occipital region as a reference would be useful for PET analysis of MSA. In contrast, the measured values of the striatum might have been affected by the atrophy. The correlation of two PET measures on the same regions, however, are robust because they are evaluated with common ROIs to cancel out the spatial effect.

Using [^{11}C]CFT and [^{11}C]RAC, we simultaneously measured presynaptic and postsynaptic nigrostriatal dopaminergic
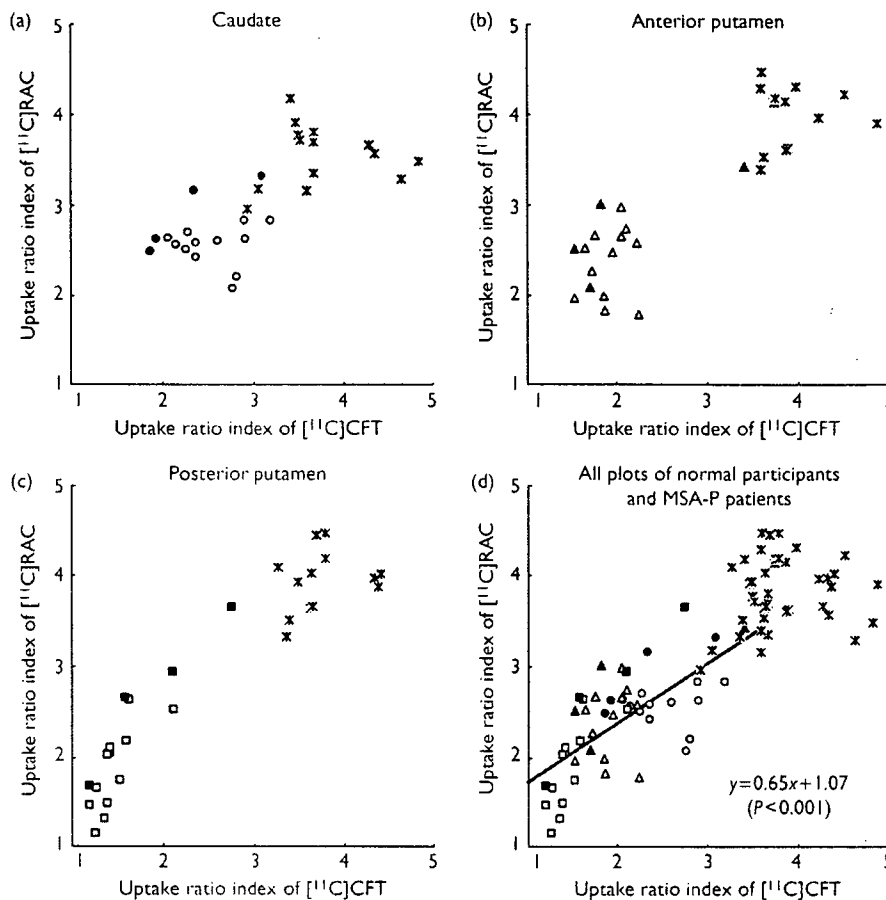
— 189 —

Fig. 2   The correlation between the uptake ratio index (URI) of [^{11}C]CFT and that of [^{11}C]RAC in the caudate nuclei (a), anterior putamen (b), posterior putamen (c), and all these areas (d) of all participants including MSA-P patients (n=8) and normal participants (n=8). The approximate lines for all the plots of the MSA-P group are shown in (d). Asterisk (*), normal participants; open circles (O), the caudate nuclei in MSA-P patients; open triangles (Δ), the anterior putamen in MSA-P patients; open squares (□), the posterior putamen in MSA-P patients; and solid markers (●), MSA-P patients exhibiting L-DOPA responsiveness. [^{11}C]CFT, ^{11}C-labeled 2β-carbomethoxy-3β-(4-fluorophenyl)-tropane; [^{11}C]RAC, ^{11}C-labeled raclopride; L-DOPA, L-3,4,dihydroxyphenyl-alanine; MSA-P, phenotype of multiple system atrophy.

functions and observed that both functions were significantly impaired in all eight patients with MSA-P compared with the normal group.

The functional impairment in the striatum was more noticeable in the putamen, particularly in its posterior part, than in the caudate nuclei. The most prominent result of our study was that a strong positive correlation was noted between presynaptic and postsynaptic functional impairments in the MSA-P group throughout the striatum regardless of the severity of the impairments. In Parkinson's disease (PD), presynaptic and postsynaptic functional impairments were reported to be negatively correlated in the putamen by PET using [^{11}C]CFT and [^{11}C]SCH 23390 (dopamine D_1-like receptor probe), reflecting severe impairment in the presynaptic marker with an upregulation of the postsynaptic function [18]. The differential diagnosis between MSA-P and PD in clinical situations is at times difficult. The patterns of presynaptic and postsynaptic functional impairments, however, demonstrated by PET contrasted between MSA-P and PD, and therefore the two disorders can be clearly differentiated with combined presynaptic and postsynaptic dopaminergic PET examinations.

Ghaemi et al. [3] applied PET using [^{18}F]FDOPA and [^{11}C]RAC to MSA-P patients and discovered that both presynaptic and postsynaptic dopaminergic functions were reduced in the nigrostriatal dopaminergic system. They did not, however, provide information about whether the impairments in the presynaptic and postsynaptic dopaminergic function were correlated in each patient. Our study is the first to demonstrate a positive correlation between the presynaptic and postsynaptic dopaminergic function with respect to the local subdivisions of the striatum and the disease duration.

What is the pathological background of the strong correlation of presynaptic and postsynaptic markers measured by PET? Pathologically, neuronal loss and gliosis are the primary forms of impairment in MSA [2]. The neuronal loss tends to be severe in both SN and striatum; however, it is not always to the same extent [1], and there has been no report regarding the correlation of pathological findings such as glial cytoplasmic inclusion [19] and α-synuclein [20,21] between SN and striatum. If the PET markers for presynaptic and postsynaptic dopaminergic function directly reflect the degree of degeneration in SN and striatum

independently, as in PD [15,22], the combination in the degree of presynaptic and postsynaptic functional impairment could be variable. The presence of a strong positive correlation between the presynaptic and postsynaptic dopaminergic functions measured by PET within patients and across patients suggests that these impairments in MSA-P are the result of the destruction of the entire synaptic structure in the striatum. Pathologically, the putamen is one of the areas with the most severe neuronal loss in MSA-P [2]. We consider that the presynaptic marker represents the degree of degeneration of the SN only if the striatum involvement is lesser than that of SN; however, once the severe destruction of striatum occurs, the presynaptic marker no longer represents the degree of SN degeneration because it is masked by the destruction of the entire structure of the synapse.

Parkinsonism in MSA is treated with L-DOPA, dopamine agonists, and anticholinergic agents; however, only a mild effect is noted in a minor population in the early stage, and the responsiveness to L-DOPA gradually disappears. Generally, responses to L-DOPA are poor in cases of MSA-P [1]. In a previous report, L-DOPA was effective in the early stage in approximately 1/3 of the MSA cases [23]. We examined two early MSA-P cases responsive to L-DOPA. In these cases, the presynaptic dopaminergic function was markedly reduced; however, the reduction in the postsynaptic dopaminergic function was relatively less severe compared with that in the cases not responsive to L-DOPA; moreover, this trend was more prominent in the striatum on the contralateral side in which L-DOPA alleviated the symptoms of parkinsonism. Churchyard et al. [24] suggested that the ineffectiveness of L-DOPA on parkinsonism in MSA is related to the dominance of neuronal loss, gliosis, and the reduction in postsynaptic dopamine D_2 receptors in the posterior putamen. Wenning et al. [5] reported that L-DOPA was highly effective in the cases in which the putamen was relatively conserved compared with the degree of nigral neuronal loss, and the effect of L-DOPA was negatively correlated with the degree of nigral degeneration, suggesting that nigral degeneration precedes striatal degeneration [1]. Whether nigral degeneration preceded striatal degeneration was not clear in our study; however, postsynaptic dopaminergic function was relatively retained in our L-DOPA-responsive cases. We consider that the degree of conservation of postsynaptic dopaminergic function is related to the effectiveness of L-DOPA in MSA-P and that a trend of dissociation of presynaptic and postsynaptic markers can be detected by PET. Further studies are necessary to increase the number of the participants and to follow up the L-DOPA-responsive cases using PET and clinical course observations.

Conclusion

We have established the presence of a strong positive correlation between the reductions in nigrostriatal presynaptic and postsynaptic dopaminergic functions and L-DOPA-responsive cases in which the degrees of presynaptic and postsynaptic functional impairments are dissociated in some manner.

The elucidation of the patterns and processes of presynaptic and postsynaptic functional impairments may provide a clue to understanding the development and advancement mechanisms of the disease and will aid in a more reliable early clinical diagnosis and prediction of drug effects.

References

1. Wenning GK, Ben-Shlomo Y, Magalhaes M, Daniel SE, Quinn NP. Clinicopathological study of 35 cases of multiple system atrophy. *J Neuro Neurosurg Psychiatry* 1995; 58:160–166.
2. James SL, Nigel L. Disorders of movement and system degeneration. In: David IG, Peter LL, editors. *Greenfield's Neuropathology.* 7th ed. Vol. 2. London: Arnold; 2002. pp. 325–430.
3. Ghaemi M, Hilker R, Rudolf J, Sobesky J, Heiss WD. Differentiating multiple system atrophy from Parkinson's disease: contribution of striatal and midbrain MRI volumetry and multi-tracer PET imaging. *J Neurol Neurosurg Psychiatry* 2002; 73:517–523.
4. Van Royen E, Verhoeff NF, Speelman JD, Wolters EC, Kuiper MA, Janssen AG. Multiple system atrophy and progressive supranuclear palsy. Diminished striatal D_2 dopamine receptor activity demonstrated by ^{123}I-IBZM single photon emission computed tomography. *Arch Neurol* 1993; 50:513–516.
5. Wenning GK, Quinn N, Magalhaes M, Mathias C, Daniel SE. 'Minimal change' multiple system atrophy. *Mov Disord* 1994; 9:161–166.
6. Gilman S, Low P, Quinn N, Albanese A, Ben-Shlomo Y, Fowler C, et al. Consensus statement on the diagnosis of multiple system atrophy. American Autonomic Society and American Academy of Neurology. *Clin Auton Res* 1998; 8:359–362.
7. Volkow ND, Fowler JS, Gatley SJ, Logan J, Wang GJ, Ding YS, et al. PET evaluation of the dopamine system of human brain. *J Nucl Med* 1996; 37:1242–1256.
8. Booij J, Tissingh G, Winogrodzka A, van Royen EA. Imaging of the dopaminergic neurotransmission system using single-photon emission tomography and positron emission tomography in patients with parkinsonism. *Eur J Nucl Med* 1999; 26:171–182.
9. Kawamura K, Oda K, Ishiwata K. Age-related changes of the [^{11}C]CFT binding to the striatal dopamine transporters in the Fischer 344 rats: a PET study. *Ann Nucl Med* 2003; 17:249–253.
10. Langer O, Nágren K, Dolle F, Lundkvist C, Sandell J, Swahn CG, et al. Precursor synthesis and radiolabelling of the dopamine D_2 receptor ligand [^{11}C]raclopride from [^{11}C]methyl triflate. *J Labelled Comp Radiopharm* 1999; 42:1183–1193.
11. Fujiwara T, Watanuki S, Yamamoto S, Miyake M, Seo S, Itoh M, et al. Performance evaluation of a large axial field-of-view PET scanner: SET-2400W. *Ann Nucl Med* 1997; 11:307–313.
12. Ardekani BA, Braun M, Hutton BF, Kanno I, Iida H. A fully automatic multimodality image registration algorithm. *J Comput Assist Tomogr* 1995; 19:615–623.
13. Gunn RN, Lammertsma AA, Hume SP, Cunningham VJ. Parametric imaging of ligand-receptor binding in PET using a simplified reference region model. *NeuroImage* 1997; 6:279–287.
14. Wong DF, Yung B, Dannals RF, Shaya EK, Ravert HT, Chen CA, et al. In vivo imaging of baboon and human dopamine transporters by positron emission tomography using [^{11}C]WIN 35 428. *Synapse* 1993; 15:130–142.
15. Frost JJ, Rosier AJ, Reich SG, Smith JS, Ehlers MD, Snyder SH, et al. Positron emission tomographic imaging of the dopamine transporter with ^{11}C-WIN 35,428 reveals marked declines in mild Parkinson's disease. *Ann Neurol* 1993; 34:423–431.
16. Antonini A, Leenders KL, Reist H, Thomann R, Beer HF, Locher J. Effect of age on D_2 dopamine receptors in normal human brain measured by positron emission tomography and ^{11}C-raclopride. *Arch Neurol* 1993; 50:474–480.
17. Mozley PD, Stubbs JB, Kung HF, Selikson MH, Stabin MG, Alavi A. Biodistribution and dosimetry of iodine-123-IBF: a potent radiolig and for imaging the D2 dopamine receptor. *J Nucl Med* 1993; 34: 1910–1917.
18. Ouchi Y, Kanno T, Okada H, Yoshikawa E, Futatsubashi M, Nobezawa S, et al. Presynaptic and postsynaptic dopaminergic binding densities in the nigrostriatal and mesocortical systems in early Parkinson's disease: a double-tracer positron emission tomography study. *Ann Neurol* 1999; 46:723–731.
19. Papp MI, Kahn JE, Lantos PL. Glial cytoplasmic inclusions in the CNS of patients with multiple system atrophy (striatonigral degeneration,

— 191 —

olivopontocerebellar atrophy and Shy–Drager syndrome). *J Neurol Sci* 1989; 94:79–100.

20. Tu PH, Galvin JE, Baba M, Giasson B, Tomita T, Leight S, et al. Glial cytoplasmic inclusions in white matter oligodendrocytes of multiple system atrophy brains contain insoluble alpha-synuclein. *Ann Neurol* 1998; 44:415–422.

21. Wakabayashi K, Yoshimoto M, Tsuji S, Takahashi H. Alpha-synuclein immunoreactivity in glial cytoplasmic inclusions in multiple system atrophy. *Neurosci Lett* 1998; 249:180–182.

22. Snow BJ, Tooyama I, McGeer EG, Yamada T, Calne DB, Takahashi H, et al. Human positron emission tomographic [^{18}F]fluorodopa studies correlate with dopamine cell counts and levels. *Ann Neurol* 1993; 34:324–330.

23. Rajput AH, Rozdilsky B, Rajput A, Ang L. Levodopa efficacy and pathological basis of Parkinson syndrome. *Clin Neuropharmacol* 1990; 13:553–558.

24. Churchyard A, Donnan GA, Hughes A, Howells DW, Woodhouse D, Wong JY, et al. Dopa resistance in multiple-system atrophy: loss of postsynaptic D$_2$ receptors. *Ann Neurol* 1993; 34:219–226.

High Occupancy of Sigma-1 Receptors in the Human Brain after Single Oral Administration of Fluvoxamine: A Positron Emission Tomography Study Using [11C]SA4503

Masatomo Ishikawa, Kiichi Ishiwata, Kenji Ishii, Yuichi Kimura, Muneyuki Sakata, Mika Naganawa, Keiichi Oda, Ryousuke Miyatake, Mihisa Fujisaki, Eiji Shimizu, Yukihiko Shirayama, Masaomi Iyo, and Kenji Hashimoto

Background: Sigma-1 receptors might be implicated in the pathophysiology of psychiatric diseases, as well as in the mechanisms of action of some selective serotonin reuptake inhibitors (SSRIs). Among the several SSRIs, fluvoxamine has the highest affinity for sigma-1 receptors ($Ki = 36$ nM), whereas paroxetine shows low affinity ($Ki = 1893$ nM). The present study was undertaken to examine whether fluvoxamine binds to sigma-1 receptors in living human brain.

Methods: A dynamic positron emission tomography (PET) data acquisition using the selective sigma-1 receptor ligand [11C]SA4503 was performed with arterial blood sampling to evaluate quantitatively the binding of [11C]SA4503 to sigma-1 receptors in 15 healthy male volunteers. Each subject had two PET scans before and after randomly receiving a single dose of either fluvoxamine (50, 100, 150, or 200 mg) or paroxetine (20 mg). The binding potential of [11C]SA4503 in 9 regions of the brain was calculated by a 2-tissue 3-compartment model. In addition, we examined the effects of functional polymorphisms of the sigma-1 receptor (SIGMAR1) gene on the binding potential of [11C]SA4503.

Results: Fluvoxamine bound to sigma-1 receptors in all brain regions in a dose-dependent manner, whereas paroxetine did not bind to sigma-1 receptors. However, there was no association between the SIGMAR1 gene polymorphism GC-241-240TT and binding potential.

Conclusions: The study demonstrated that fluvoxamine bound to sigma-1 receptors in living human brain at therapeutic doses. These findings suggest that sigma-1 receptors may play an important role in the mechanism of action of fluvoxamine.

Selective serotonin reuptake inhibitors (SSRIs) have emerged as a major therapeutic advance in psychopharmacology. SSRIs are the treatment of choice for many indications, including major depressive disorder, dysthymia, obsessive-compulsive disorder, and obsessive-compulsive disorder spectrum disorders (which include panic disorder, eating disorders, and others), because of their efficacy, safety profile, tolerability, and low toxicity in case of overdose, as well as patient compliance (1,2). Although all the SSRIs share the blockade of the serotonin transporters that leads to elevation of serotonin levels throughout the central nervous system, it is well known that their pharmacology is quite heterogenous (3–11).

Sigma-1 receptors act as specific binding sites in the central nervous system, and they exert a potent modulation on a number of neurotransmitter systems, including the glutamatergic, norad-

renergic, dopaminergic, serotonergic and cholinergic systems. Several lines of evidence suggest that sigma-1 receptors play a role in the pathophysiology of responses to stress and psychiatric diseases, including major depression, schizophrenia, cognition, and addiction (12–17). Cell biologically, sigma-1 receptors mainly reside on the endoplasmic reticulum and regulate Ca^{2+} signaling (18). Furthermore, sigma-1 receptors form a complex with the cytoskeletal adaptor protein ankyrin, and with stimulation to the sigma-1 receptor, it translocates to nuclear membranes and plasma membranes, suggesting that sigma-1 receptors have an important role in neuroplasticity (19). Narita et al. (3) reported that some SSRIs possess high to moderate affinities for sigma-1 receptors in rat brain. The rank order of affinity of SSRIs for sigma-1 receptors is as follows: fluvoxamine ($Ki = 36$ nM) > sertraline ($Ki = 57$ nM) > fluoxetine ($Ki = 120$ nM) > citalopram ($Ki = 292$ nM). In contrast, paroxetine ($Ki = 1893$ nM) has low affinity for sigma-1 receptors (3). Thus, it seems that sigma-1 receptors may play a role in the mechanism of action of some SSRIs, such as fluvoxamine (3,15,20).

Positron emission tomography (PET) is the most effective technique to estimate the receptor occupancy rates of drugs in human brain (21,22). Recently, it has been demonstrated that [11C]SA4503 is a selective PET ligand for sigma-1 receptor in the brain (23–26). SA4503 has an affinity of approximately 17.4 nM (IC_{50}) for the sigma-1 receptor, which is about 100 times higher than those for sigma-2, α_1-adrenergic, dopamine D_2, serotonin (5-HT)$_{1A}$, 5-HT$_2$, histamine H_1, muscarinic M_1, and muscarinic M_2 receptors, and has no affinity for other 29 receptors, ion channels, and second messenger systems (27). The inhibition curves of SA4503 for [3H](+)pentazocine binding were shifted to the

From the Division of Clinical Neuroscience (MIs, KH), Chiba University Center for Forensic Mental Health; Graduate School of Information Science (MS), Nara Institute of Science and Technology; Japan Society for the Promotion of Science (MN); Department of Psychiatry (MIs, RM, MF, ES, YS, MIy), Chiba University Graduate School of Medicine, Chiba; Positron Medical Center (MIs, KI, KI, YK, MN, KO), Tokyo Metropolitan Institute of Gerontology, Tokyo, Japan.

Address reprint requests to Kenji Hashimoto, Ph.D., Division of Clinical Neuroscience, Chiba University Center for Forensic Mental Health, 1-8-1 Inohana, Chiba 260-8670, Japan; E-mail: hashimoto@faculty.chiba-u.jp.

right in the presence of GTPγS, as similar to those of sigma-1 receptor agonists[(+)-3-PPP and (+)-pentazocine] (27). In addition, similar to sigma-1 receptor agonists [(+)-3-PPP and (+)-pentazocine], SA4503 significantly increased the Kd value, but not the Bmax value, for specific [³H](+)pentazocine binding to sigma-1 receptors (27). These findings suggest that SA4503 is a sigma-1 receptor agonist (27). Binding of [¹¹C]SA4503 in the brains of patients with Alzheimer's or Parkinson's disease has been shown to be lower than in normal controls (15,28). Furthermore, Ishiwata *et al.* (29) reported a high occupancy of sigma-1 receptors (approximately 80%) as well as dopamine D_2 receptors (approximately 60%) in human brain after a single oral administration of the typical antipsychotic drug haloperidol (3 mg), suggesting that PET study using [¹¹C]SA4503 can be used for evaluating the sigma-1 receptor occupancy rates by therapeutic drugs in human brain (29).

The purpose of this study was to determine whether two SSRIs, fluvoxamine and paroxetine, bind to sigma-1 receptors in human brain by using [¹¹C]SA4503 and PET. In addition, we examined the effects of polymorphisms of the sigma-1 receptor (SIGMAR1; OMIM No. 601978) gene on the binding potential of [¹¹C]SA4503 in human brain, since polymorphisms (T-485A and GC-241-240TT; rs1799729) in the SIGMAR1 gene have been shown to be functional polymorphisms (30).

Methods and Materials

Subjects

This study was approved by the Ethical Committee of Tokyo Metropolitan Institute of Gerontology and the Ethics Committee of Chiba University Graduate School of Medicine. Fifteen healthy male volunteers participated in the study (mean age = 34.7 years, SD = 4.6, range = 28–41). Written informed consent was obtained from each subject after the procedures had been fully explained. None of the subjects had any neurological or psychological findings, or showed any abnormalities in the brain magnetic resonance imaging (MRI) scan taken between the two PET scans. None had been receiving any medications of any kind. None had a history of alcoholism.

[¹¹C]SA4503 and PET

Each volunteer participated in two [¹¹C]SA4503-PET scans, one before and one after oral administration of an SSRI. The SSRI was administered within 5 min after the end of the first PET scan. The second PET scan took place 4–4.5 hours after taking the SSRI to achieve an adequate level of drug concentration in blood. It has been reported that after oral administration of a single dose of fluvoxamine (50 mg) in healthy subjects, the concentration in blood reaches its peak in approximately 5–6 hours (31,32). Accordingly, we collected blood samples just before tracer injection of the second PET scan to monitor the concentration of fluvoxamine. The concentration of fluvoxamine in blood was measured by liquid chromatography followed by tandem mass spectrometry.

The volunteers were randomly administered either fluvoxamine (50, 100, 150 or 200 mg, n = 3; Luvox (Astellas Ltd, Tokyo, Japan) or paroxetine (20 mg, n = 3; Paxil (GlaxoSmithKline Ltd, Tokyo, Japan). All drug tablets were sealed in the same nondescript capsule so that both the volunteers and administrator would be blind to the contents. PET was performed at the Positron Medical Center, Tokyo Metropolitan Institute of Gerontology with a SET 2400W scanner (Shimadzu Co., Kyoto, Japan)

(30,33). The spatial resolution was 4.4 mm full width at half maximum in the transverse direction and 6.5 mm full width at half maximum in the axial direction; the image matrix was 128 × 128 × 50 and the voxel size was 2 × 2 × 3.125 mm. [¹¹C]SA4503 was prepared as described previously (21,23). The injected doses of [¹¹C]SA4503 were 9.3 ± 2.1 MBq/.18 ± .16 nmol/kg (specific activity 79 ± 42 TBq/mmol). A transmission scan was performed with a rotating ⁶⁸Ga/⁶⁸Ge rod source for 5 min for attenuation correction before the administration of the tracer. A dynamic series of decay-corrected PET data acquisition was performed in the 2-dimensional mode for 90 min starting at the time of the intravenous bolus injection of [¹¹C]SA4503. The frame arrangement was 10 sec × 6 frames, 30 sec × 3 frames, 60 sec × 5 frames, 150 sec × 5 frames, and 300 sec × 14 frames. The dynamic image was reconstructed with a filtered back-projection algorithm using a Butterworth filter (1.25 cycles/cm, order 2).

Each subject was placed in a supine position with eyes closed. Immediately after the bolus injection, 12 arterial blood samples were collected at 10-sec intervals over 2 min, the next 2 samples were collected at 15-sec intervals over 30 sec, and the remaining 12 samples were collected at longer intervals, for a total of 26 samples. All samples were manually drawn. Plasma was separated, weighed and measured for radioactivity with a sodium iodide (Tl) well scintillation counter. Five samples collected at 3, 10, 20, 30, and 40 min were further processed by high performance liquid chromatography for metabolite analysis (23,34).

Data Analysis

Image manipulations were carried out on an O2 work station (Silicon Graphics Inc., Mountain View, California), using the medical image processing application package "Dr. View," version 5.2 (AJS Co. Ltd., Tokyo, Japan). Regions of interest were defined over the frontal, temporal, parietal, occipital, and anterior cingulate cortices, head of the caudate nucleus, putamen, thalamus, and cerebellum with reference to the coregistered MRI, which served as an anatomical guide.

Binding of [¹¹C]SA4503 to sigma-1 receptors was calculated as the binding potential by methods described elsewhere (34). Briefly, binding potentials were computed using a 2-tissue 3-compartment model (35). Sigma-1 receptor occupancy (%) by SSRI was calculated for each region of interest as 100' [(binding potential at baseline–binding potential at SSRI-loading)/binding potential at baseline]. Images of the distribution volumes of [¹¹C]SA4503 were calculated using the Logan plot method (34,36).

The relationship between sigma-1 receptor occupancy and the dose or blood concentration of fluvoxamine was modeled by the equation $Occ = a \, (F/(F + ED50))$, where Occ refers to occupancy, F refers to dose or blood level of fluvoxamine, a is the maximal receptor occupancy and ED50 is the blood fluvoxamine level resulting in 50% maximal receptor occupancy.

Genotype Analysis

The genotypes of the T-485A and GC-241-240TT in the 5' untranslated region of the SIGMAR1 gene was analyzed in all volunteers according to methods previously described (30,37).

Statistical Analysis

The data are the mean ± SD. Statistical analysis was performed by using the software package SPSS (SPSS 12.0J; SPSS, Inc., Tokyo, Japan). The dose-dependent relationship was evaluated by one-way analysis of variance with contrast (polynomial). The relationship between the binding potential at baseline